Moiré excitons in biased twisted bilayer graphene under pressure

V. G. M. Duarte,[1,*] D. R. da Costa,[2,†] N. M. R. Peres,[3,4,5,‡] L. K. Teles,[1,§] and A. J. Chaves[1,‖]

[1]*Departamento de Física, Instituto Tecnológico de Aeronáutica, 12228-900, São José dos Campos, SP, Brazil*

[2]*Departamento de Física, Universidade Federal do Ceará, 60455-900, Fortaleza, CE, Brazil*

[3]*Centro de Física das Universidades do Minho e do Porto (CF-UM-UP) e Departamento de Física, Universidade do Minho, P-4710-057 Braga, Portugal*

[4]*International Iberian Nanotechnology Laboratory (INL), Avenida Mestre José Veiga, 4715-330 Braga, Portugal*

[5]*POLIMA—Center for Polariton-driven Light-Matter Interactions, University of Southern Denmark, Campusvej 55, DK-5230 Odense M, Denmark*

(Received 18 October 2023; revised 31 May 2024; accepted 14 June 2024; published 3 July 2024)

Using the tight-binding model, we report a gap opening in the energy spectrum of a twisted bilayer graphene under the application of pressure, that can be further amplified by the presence of a perpendicular bias voltage. The valley edges are located along the K-Γ path of the superlattice Brillouin zone, with the band gap reaching values up to 200 meV in the single-particle picture. Employing the formalism of the semiconductor Bloch equations, we observe an enhancement of the band gap due to the electron-electron interaction, with a renormalization of the band gap of about 160 meV. From the solution of the corresponding Bethe-Salpeter equation, we show that this system supports highly anisotropic bright excitons whose electrons and holes are strongly hybridized between the adjacent layers.

DOI: 10.1103/PhysRevB.110.035405

I. INTRODUCTION

Moiré patterns naturally appear in overlaying crystals with different individual lattice parameters or even in homobilayer when they are slightly offset due to rotation [1,2], such as turbostratic graphite owed to orientation disorder [3]. Several extraordinary phenomena have been studied in different twisted materials, such as superconductivity and flat bands, in what is called magic angle in twisted bilayer graphene (TBG) [4–6], Mott-like insulating states in half-filling TBG [7], room-temperature ferroelectricity in twisted bilayer MoS_2 [8], an alternation between ferromagnetic to antiferromagnetic domains in twisted bilayer CrI_3 [9], and Hubbard physics in twisted bilayer WSe_2 [10].

For vertical stacked two-dimensional (2D) semiconductor materials with a twist, e.g., rotated transition metal dichalcogenides' (TMDs) bilayers, the periodic long-range interaction, known as the moiré potential [11], results in a modulation of the band edge energies [12]. In addition, tremendous interest in exciton physics bloomed with the advent of 2D materials due to their high binding energies [13], stemming from reduced screening and lower dimensionality [14]. In this context, recent experiments have demonstrated that such structural moiré patterns can trap long-lived and valley-polarized interlayer excitons, referred to as moiré excitons [15–19]. Those excitons have a wide range of possible applications, including the development of arrays of quantum emitters [20] and excitonic devices [21].

Since 2006, the band-gap tunability of the AB-stacked bilayer graphene with a perpendicular electric field has been well documented [22–24]. This discovery triggered fundamental interest in exploring optical properties dominated by bound states. An additionally reported route to open a band gap in biased Bernal stacked bilayer graphene is by nanomechanical control, achieved, for instance, via interlayer distance decrease [25]. The electrostatic control of electronic TBG bands and the possibility of band-gap tuning were theoretically explored [26] for sublattice-exchange-dependent commensurate TBG with different interlayer shift vectors.

The excitonic physics of bilayer graphene has been extensively explored. For AB-stacked bilayer graphene, theoretical predictions [27–30] of tunable excitons date back to 2010, and experimental demonstrations [29] in 2017 showcased the formation of excitons with large binding energies and distinct optical selection rules. Conversely, for TBG, despite the observation of excitonic resonances in the continuum [31] and prediction of electron-hole bound states between Landau levels [32], nonmagnetic excitons in semiconductor TBG have not been predicted or observed to date.

Therefore, motivated by the experimental advances in the twist physics on the moiré excitons hosted in artificially engineered homobilayer [33] and heterobilayer [34] TMDs, that have revealed twist angle dependence in the excitonic properties and whose layer hybridization can be controlled by external electric field [34], in this paper, we examine routes for the formation of excitons in TBG. To achieve that, using a tight-binding model within a single-particle picture, we first demonstrate gap opening in TBG under pressure and bias voltage for certain twist angles that generate commensurate

*Contact author: victor.duarte@ga.ita.br
†Contact author: diego_rabelo@fisica.ufc.br
‡Contact author: peres@fisica.uminho.pt
§Contact author: lkteles@ita.br
‖Contact author: andrejck@ita.br

unit cells, which suggests the possibility of exciton formation in bilayer graphene with a twist. Recently, pressure was applied in twisted TMDs to tune minibands and interlayer coupling [35,36], which corroborates the feasibility of our proposal in TBG. Our analysis reveals that the single-particle bands are highly hybridized between different layers near the band edge. To appropriately describe the exciton formation, many-body interactions are added to the model, leading to the dielectric function calculation in the context of the random phase approximation (RPA) [37–39], adapting the Adler-Wiser formula [40,41] to account for the polarized screening effect between the two layers in 2D systems. Next, we evaluate the exchange self-energy, which renormalizes the optical band and corrects the band gap by accounting for the electron-electron interaction [42,43]. As shall be discussed, our results clearly show a sixfold symmetric optical band with six nonequivalent band edges, where the lowest-energy exciton wave functions are localized.

II. TIGHT-BINDING MODEL

It was recently shown [44] that the geometric relaxation of atoms can be safely neglected for twist angles above 1.8°, which theoretically ensures us to limit discussing large angle cases with rigid rotation features. Hence, a large twist angle TBG lattice can be safely modeled as two stacked graphene lattices with a rigid vertical translation d in the out-of-plane axis and a rigid in-plane rotation θ. In this section, we present our approach for the modeling of noninteracting electrons in TBG, considering a rigid structure of two planar layers with interlayer distance d. The unit cell of TBG is well defined (commensurate) for twist angles that obey the equation [45–48]

$$\theta(p,q) = \arccos\left(\frac{3p^2+3pq+q^2/2}{3p^2+3pq+q^2}\right), \tag{1}$$

where p, q are integers. Further details of the crystallographic structure of TBG are presented in Appendix A.

A. Formalism

Our description is based on the tight-binding approximation for the energetically dominant TBG orbitals, p_z, in the vicinity of the energy levels on TBG band edges. The tight-binding Hamiltonian in the second quantization formalism can be written as

$$\mathcal{H}_{\rm TB} = \sum_{\ell\ell'}\sum_{\boldsymbol{\delta}_\ell\boldsymbol{\delta}_{\ell'}}\sum_{\mathbf{R}\mathbf{R}'} t(\mathbf{R}+\boldsymbol{\delta}_\ell-\mathbf{R}'-\boldsymbol{\delta}'_{\ell'})c^\dagger_{\mathbf{R}+\boldsymbol{\delta}_\ell}c_{\mathbf{R}'+\boldsymbol{\delta}_{\ell'}}, \tag{2}$$

where $t(\mathbf{r})$ is the transfer integral [49,50], $c^\dagger_{\mathbf{r}}$ ($c_{\mathbf{r}}$) is the fermionic operator that creates (annihilates) a p_z electron centered at $\mathbf{r}$, $\ell = 1$ (2) labels the bottom (top) layer, $\boldsymbol{\delta}_\ell$ is a basis vector on layer ℓ, and $\mathbf{R}$ is a superlattice vector. By assuring commensurability [Eq. (1)], the atomic structure of TBG is guaranteed to be periodic, which allows us to introduce the Fourier transform

$$c^\dagger_{\mathbf{R}+\boldsymbol{\delta}_\ell} = \frac{1}{\sqrt{N}}\sum_{\mathbf{k}}^{\rm BZ} e^{i\mathbf{k}\cdot(\mathbf{R}+\boldsymbol{\delta}_\ell)}b^\dagger_{\mathbf{k}\boldsymbol{\delta}_\ell}, \tag{3}$$

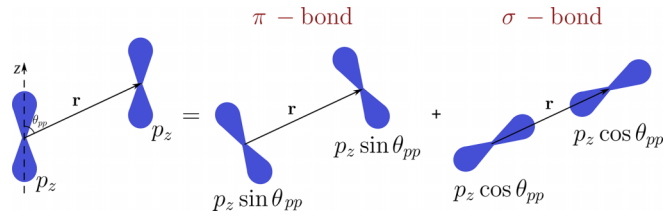

FIG. 1. Illustration of the interactions between a pair of p_z orbitals, decomposed into π- and σ-like interactions. The lobes are projected onto a pair of axes, one parallel and one perpendicular to the vector $\mathbf{r}$ connecting the orbital centers.

where N is the number of unit cells of the material, $b^\dagger_{\mathbf{k}\boldsymbol{\delta}_\ell}$ is the Fourier transformed operator, and $\sum_{\mathbf{k}}^{\rm BZ}$ is a sum over wave vectors $\mathbf{k}$ restricted to the first Brillouin zone (BZ). The Hamiltonian (2), rewritten in momentum space, is

$$\mathcal{H}_{\rm TB} = \sum_{\mathbf{k}}^{\rm BZ}\sum_{\ell\ell'}\sum_{\boldsymbol{\delta}_\ell\boldsymbol{\delta}_{\ell'}}\sum_{\mathbf{R}} e^{i\mathbf{k}\cdot(\mathbf{R}+\boldsymbol{\delta}_\ell-\boldsymbol{\delta}_{\ell'})}t(\mathbf{R}+\boldsymbol{\delta}_\ell-\boldsymbol{\delta}_{\ell'})b^\dagger_{\mathbf{k}\boldsymbol{\delta}_\ell}b_{\mathbf{k}\boldsymbol{\delta}_{\ell'}}. \tag{4}$$

We emphasize the importance of deriving a formulation for the Hamiltonian on a finite basis. This allows us to numerically construct and diagonalize Hamiltonian matrices. Here, we used the finite set of vectors, $\boldsymbol{\delta}_\ell$, to label this basis, taking the periodicity of the infinite system into account. As shall be discussed later in this section, the transfer integrals are position-dependent functions that decay exponentially with distance. Thus, the infinite sum over lattice vectors, $\sum_{\mathbf{R}}$, in Eq. (4) can be safely truncated.

In the tight-binding picture, the transfer integrals $t(\mathbf{r})$ describe the energy parameters associated with the hoppings of electrons between different atomic sites. Here, we consider one orbital (p_z) per atomic site. Since the p_z orbitals do not all align vertically due to the presence of two stacked graphene layers, geometrical spatial aspects of the p_z orbital distribution must be considered.

If $\mathbf{r}$ is the distance vector between two p_z orbitals, then $\cos\theta_{pp} = (\mathbf{r}\cdot\mathbf{e}_z)/r$ is the cosine of the angle that $\mathbf{r}$ forms with the z axis. Each p_z orbital can be decomposed into a $p_z\cos\theta_{pp}$ component in the direction parallel to $\mathbf{r}$, and a $p_z\sin\theta_{pp}$ component in the orthogonal direction. The $p_z\cos\theta_{pp}$–$p_z\cos\theta_{pp}$ and $p_z\sin\theta_{pp}$–$p_z\sin\theta_{pp}$ interactions resemble a σ bond and a π bond, respectively, as illustrated in Fig. 1. Orthogonal interactions $p_z\cos\theta_{pp}$–$p_z\sin\theta_{pp}$ vanish due to the opposite signs of the p_z orbital globes. Denoting the pure σ- and π-like transfer integrals by $V_{pp\sigma}(r)$ and $V_{pp\pi}(r)$, the transfer integral in Slater-Koster form becomes [49–51]

$$t(\mathbf{r}) = V_{pp\sigma}(r)\cos^2\theta_{pp} + V_{pp\pi}(r)\sin^2\theta_{pp}. \tag{5}$$

Using the trigonometric identity $\sin^2\theta_{pp} = 1-\cos^2\theta_{pp}$ and $\cos\theta_{pp}$ definition, Eq. (5) becomes

$$t(\mathbf{r}) = V_{pp\sigma}(r)\left(\frac{\mathbf{r}\cdot\mathbf{e}_z}{r}\right)^2 + V_{pp\pi}(r)\left[1-\left(\frac{\mathbf{r}\cdot\mathbf{e}_z}{r}\right)^2\right]. \tag{6}$$

Atomic orbitals have exponentially decaying tails far from their centers. For this reason, the pure σ and π transfer integrals are also assumed to decay exponentially. Thus, they can

be modeled as exponential functions with fitting parameters chosen to reflect the physical properties of the real system. Following the results of Ref. [52], the pure transfer integrals in Eq. (6) are fitted as

$$V_{pp\pi}(r) = V^0_{pp\pi} \exp\left(-\frac{r - a_{cc}}{\delta_0}\right), \tag{7a}$$

$$V_{pp\sigma}(r) = V^0_{pp\sigma} \exp\left(-\frac{r - d_0}{\delta_0}\right), \tag{7b}$$

where $a_{cc} = a/\sqrt{3} \approx 1.42$ Å is the carbon-carbon bond length and $d_0 \approx 3.35$ Å is the strain-free interlayer distance. The intralayer and interlayer nearest-neighbor hoppings are, respectively, given by

$$V_{pp\pi}(a_{cc}) = V^0_{pp\pi} \approx -2.7 \text{ eV}, \tag{8}$$

$$V_{pp\sigma}(d_0) = V^0_{pp\sigma} \approx 0.48 \text{ eV}, \tag{9}$$

being set to agree with monolayer graphene and AB-stacked bilayer graphene band structures, respectively. The decay length $\delta_0 = 0.148a$ modulates how fast the exponential functions go to zero. To truncate the sum $\sum_{\mathbf{R}}$ in Eq. (4) preserving a correct physical description of intra- and interlayer coupling in TBG, we must identify the dominant intra- and interlayer hopping terms. Following Ref. [52], we restrict intralayer hoppings to the nearest intralayer neighbors, and the interlayer ones to atomic distances of $r \leqslant 4a_{cc}$.

It is worth emphasizing that applying any strain or pressure in a crystal modifies the vectors connecting lattice sites and changes the corresponding hopping parameters. Note that the transfer integral (6) is a position-dependent term, implying hopping variations by lattice changes. Here, since we assume rigid structures, TBG under pressure can be simply modeled by uniformly varying the interlayer distance.

By applying a uniform electric field $\boldsymbol{\mathcal{E}} = \mathcal{E}\mathbf{e}_z$ perpendicular to TBG, a vertical electric potential $v(z) = v(0) - \mathcal{E}z$ is induced. We set the reference $v(d/2) = 0$, such that the potentials at the graphene layers are $v(0) = \mathcal{E}d/2$ and $v(d) = -\mathcal{E}d/2$. Thus, within the tight-binding approach, the bias voltage is included as an on-site potential given by the diagonal term [53]

$$\mathcal{H}_V = \sum_{\mathbf{R}} \sum_{\ell\boldsymbol{\delta}_\ell} \frac{V}{2} s_\ell c^\dagger_{\mathbf{R}+\boldsymbol{\delta}_\ell} c_{\mathbf{R}+\boldsymbol{\delta}_\ell} = \sum_{\mathbf{k}}^{\text{BZ}} \sum_{\ell\boldsymbol{\delta}_\ell} \frac{V}{2} s_\ell b^\dagger_{\mathbf{k}\boldsymbol{\delta}_\ell} b_{\mathbf{k}\boldsymbol{\delta}_\ell}, \tag{10}$$

where $s_\ell = \delta_{\ell 1} - \delta_{\ell 2}$ and $V = -e[v(d) - v(0)] = e\mathcal{E}d$ is the total electric potential energy difference between the adjacent graphene layers.

Combining Eqs. (4) and (10), we obtain the complete single-particle Hamiltonian for the noninteracting p_z electrons of TBG under an external perpendicular electric field,

$$\mathcal{H}_0 = \mathcal{H}_{\text{TB}} + \mathcal{H}_V = \sum_{\mathbf{k}}^{\text{BZ}} \sum_{\ell\ell'} \sum_{\boldsymbol{\delta}_\ell\boldsymbol{\delta}_{\ell'}} h_{\boldsymbol{\delta}_\ell\boldsymbol{\delta}_{\ell'}}(\mathbf{k}) b^\dagger_{\mathbf{k}\boldsymbol{\delta}_\ell} b_{\mathbf{k}\boldsymbol{\delta}_{\ell'}}, \tag{11}$$

where we defined the matrix element

$$h_{\boldsymbol{\delta}_\ell\boldsymbol{\delta}_{\ell'}}(\mathbf{k}) = \frac{V}{2} s_\ell \delta_{\ell\ell'} \delta_{\boldsymbol{\delta}_\ell\boldsymbol{\delta}_{\ell'}} + \sum_{\mathbf{R}} e^{i\mathbf{k}\cdot(\mathbf{R}+\boldsymbol{\delta}_\ell-\boldsymbol{\delta}_{\ell'})} t(\mathbf{R} + \boldsymbol{\delta}_\ell - \boldsymbol{\delta}_{\ell'}). \tag{12}$$

To diagonalize $\mathcal{H}_0$, we introduce the Bloch operator

$$a^\dagger_{n\mathbf{k}} = \sum_{\boldsymbol{\delta}_\ell} u_{n\boldsymbol{\delta}_\ell}(\mathbf{k}) b^\dagger_{\mathbf{k}\boldsymbol{\delta}_\ell}, \tag{13}$$

where n is the band label and the Bloch functions $u_{n\boldsymbol{\delta}_\ell}(\mathbf{k})$ form an orthonormal basis. The inverse relation is

$$b^\dagger_{\mathbf{k}\boldsymbol{\delta}_\ell} = \sum_{n} u^*_{n\boldsymbol{\delta}_\ell}(\mathbf{k}) a^\dagger_{n\mathbf{k}}. \tag{14}$$

Substituting Eq. (14) in Eq. (11), one gets

$$\mathcal{H}_0 = \sum_{\mathbf{k}}^{\text{BZ}} \sum_{\ell\ell'} \sum_{\boldsymbol{\delta}_\ell\boldsymbol{\delta}_{\ell'}} \sum_{nn'} h_{\boldsymbol{\delta}_\ell\boldsymbol{\delta}_{\ell'}}(\mathbf{k}) u^*_{n\boldsymbol{\delta}_\ell}(\mathbf{k}) u_{n'\boldsymbol{\delta}_{\ell'}}(\mathbf{k}) a^\dagger_{n\mathbf{k}} a_{n'\mathbf{k}}. \tag{15}$$

Since $\mathcal{H}_0$ must be diagonal in the basis $a^\dagger_{n\mathbf{k}}$, Eq. (15) can be split into the following pair of equations:

$$\sum_{\ell\ell'} \sum_{\boldsymbol{\delta}_\ell\boldsymbol{\delta}_{\ell'}} h_{\boldsymbol{\delta}_\ell\boldsymbol{\delta}_{\ell'}}(\mathbf{k}) u^*_{n\boldsymbol{\delta}_\ell}(\mathbf{k}) u_{n'\boldsymbol{\delta}_{\ell'}}(\mathbf{k}) = E_{n\mathbf{k}} \delta_{nn'}, \tag{16a}$$

$$\mathcal{H}_0 = \sum_{\mathbf{k}}^{\text{BZ}} \sum_{n} E_{n\mathbf{k}} a^\dagger_{n\mathbf{k}} a_{n\mathbf{k}}, \tag{16b}$$

where the eigenvalues $E_{n\mathbf{k}}$ describe the energy bands of the system. The Hamiltonian in the diagonal form (16b) will be important for further derivations in this work. To obtain the energy bands and Bloch functions, one should solve the eigenvalue problem (16a). For that purpose, using the orthonormality of the basis of functions $u_{n\boldsymbol{\delta}_\ell}(\mathbf{k})$, we can rewrite Eq. (16a) in the standard form

$$\sum_{\ell'\boldsymbol{\delta}_{\ell'}} h_{\boldsymbol{\delta}_\ell\boldsymbol{\delta}_{\ell'}}(\mathbf{k}) u_{n\boldsymbol{\delta}_{\ell'}}(\mathbf{k}) = E_{n\mathbf{k}} u_{n\boldsymbol{\delta}_\ell}(\mathbf{k}). \tag{17}$$

To numerically solve Eq. (17), explicit values for $\mathbf{k}$ must be sampled, as illustrated by small green dots in Fig. 9(b). For that, we sampled $\mathbf{k}$ points, discretizing the momentum space, in the hexagonal sampling $\mathbf{k}$ region highlighted in Fig. 9(b). Any valid reciprocal unit cell with the same area as the first Brillouin zone could be chosen; for instance, the rectangular sampling region illustrated with small gray symbols in Fig. 9(b), where we could assume a rectangular grid with N_i sampling points in the $i = x', y'$ directions. Within such rectangular discretization, the sampling points can be explicitly written as

$$\mathbf{k}^{(i)}_{n_{x'}n_{y'}} = \left(\frac{n_{x'}}{N_{x'}}\frac{\sqrt{3}}{2}\mathbf{G}_2 \cdot \mathbf{e}_y + \frac{n_{y'}}{N_{y'}}\mathbf{G}_2 \cdot \mathbf{e}_x\right)\mathbf{e}_x + \left(\frac{n_{y'}}{N_{y'}}\mathbf{G}_2 \cdot \mathbf{e}_y - \frac{n_{x'}}{N_{x'}}\frac{\sqrt{3}}{2}\mathbf{G}_2 \cdot \mathbf{e}_x\right)\mathbf{e}_y, \tag{18}$$

where $n_i = 0, 1, 2, \ldots, N_i - 1$. In this manner, the total number of sampling points, $N_{\mathbf{k}} = N_{x'}N_{y'}$, will also act as the number of unit cells that constitute our material. $N_{\mathbf{k}}$ is also directly related to the chosen convergence parameter since the larger the $N_{\mathbf{k}}$, the higher the expected accuracy. Instead of the equivalent discussed rectangular unit cell, we use the hexagonal Brillouin zone with a triangular grid suggested by

the C_6 symmetry of the system, as also shown in Fig. 9. The points of such a grid are described by the equation

$$\mathbf{k}_{n_1 n_2} = \frac{n_1(2\mathbf{G}_1 + \mathbf{G}_2) + n_2(\mathbf{G}_1 + 2\mathbf{G}_2)}{3(N_h - 1)}, \tag{19}$$

where N_h is a positive integer, and n_1, n_2 is any pair of integers such that $-N_h < n_1, n_2 < N_h$ and $|n_1 + n_2| < N_h$. The total number of grid points, $N_{\mathbf{k}} = 3N_h(N_h - 1) + 1$, is regulated monotonically by N_h.

As will be shown later, it will be necessary to evaluate the single-particle wave function $u_{n\delta_\ell}(\mathbf{k})$ at points $\mathbf{k}$ in the six Brillouin zones adjacent to the first Brillouin zone. However, we know that $u_{n\delta_\ell}(\mathbf{k})$ is periodic in reciprocal space, following the rule

$$u_{n\delta_\ell}(\mathbf{k}) = u_{n\delta_\ell}(\mathbf{k} + m_1\mathbf{G}_1 + m_2\mathbf{G}_2), \tag{20}$$

for any pair of integers m_1, m_2. Additionally, the relation

$$\mathbf{k}_{n_1 n_2} + m_1\mathbf{G}_1 + m_2\mathbf{G}_2 = \mathbf{k}_{n_1' n_2'} \tag{21}$$

holds for

$$n_1' = n_1 + (N_h - 1)(2m_1 - m_2), \tag{22a}$$

$$n_2' = n_2 + (N_h - 1)(2m_2 - m_1). \tag{22b}$$

For our purposes, Eq. (21) will be restricted to values of m_1, m_2 that shift the grid points $\mathbf{k}_{n_1 n_2}$ in the first Brillouin zone to the six Brillouin zones adjacent to it, i.e., $(m_1, m_2) = (1, 0), (0, 1), (-1, 0), (0, -1), (1, 1), (-1, -1)$.

B. Band-gap opening in single-particle TBG spectrum

The single-particle Hamiltonian (11) describes biased TBG's noninteracting p_z electrons under pressure. The Hamiltonian depends on the parameters p, q, V, and d. The integers p, q vary the twist angle $\theta(p, q)$, therefore changing the relative atomic positions and interactions. The electric bias V adjusts the gate voltage between the TBG layers, thereby opening the possibility for band-gap formation. At last, the interlayer distance d mimics the effect of exerting vertical pressure in TBG, which changes its interlayer distance away from the equilibrium configuration ($d = d_0 = 3.35$ Å), therefore also changing the interlayer atomic relative positions and interactions. For the numerical calculation, we also have the integer N_i, which monotonically regulates the number of sampled $\mathbf{k}$ points in the BZ, which allows one to study momentum space convergence. No changes due to pressure are considered on the intralayer hoppings, i.e., we will neglect the Poisson ratio. For sufficiently small unit cells, the eigenvalue problem (17) can be solved in momentum space for each sampled $\mathbf{k}$ point. In addition to experimental concerns that may break the rigid TBG model, such as static stability and atom reconfiguration, the need for small unit cells also brings a computational concern that motivated us to restrict our discussion to large angles. In fact, the overall increase in the number of atoms per unit cell (unit cell number) with decreasing twist angle puts a limit to the dimension of Hamiltonians that we can exactly diagonalize.

We present, in Fig. 2, the electronic band gap of TBG for all the commensurable twist angles (1) that generate unit cells of less than 500 atoms, as a function of the bias potential and the interlayer distance. In general, one can notice the following: (i) highly twisting angle-dependent metallic-to-semiconductor transition induced solely by pressure, an external electric field, or the combination of them; and (ii) $\theta(1, 3k)$ ($k \in \mathbb{Z}$) twist angles exhibit a particular gap tendency, increasing as d decreases, until some optimal value where the gap is maximum. This optimal point is brought closer to the equilibrium interlayer distance line $d = d_0$ as V increases. This tunability of the maximum band gap through the external bias enhances the prospects for experimental reproduction of this behavior *in situ*, demanding lower pressures more feasibly reached in experiments.

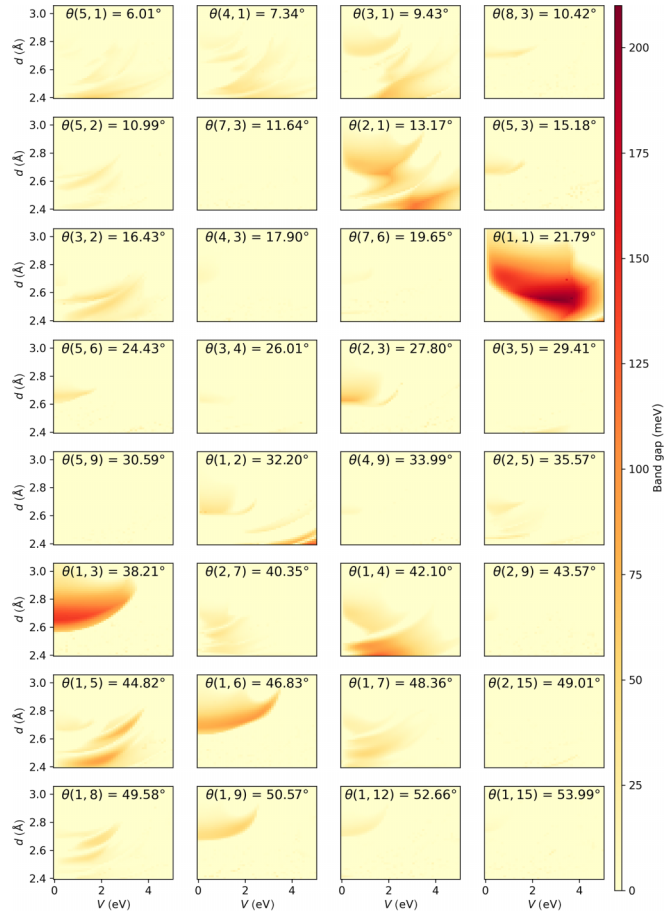

FIG. 2. Contour plots of the band gap induced in TBG due to interlayer distance d changes with respect to the equilibrium position d_0, mimicking the application of vertical pressure, and under a perpendicularly applied electric field with bias voltage V, for all twist angles that generate commensurate unit cells with less than 500 atoms.

Figures 3(a) and 3(b) show color plots of the single-particle band-gap dependence on the interlayer distance d and the external bias V for a TBG with twist angle (a) $\theta(1, 1) = 21.79°$ and (b) $\theta(1, 6) = 46.83°$. Our findings demonstrate, in certain configurations, band gaps of up to 0.2 eV when one combines electric bias and pressure, although just one of them is enough to generate a gap opening in some cases, as shown in Fig. 2. Therefore, it turns TBG into a narrow gap semiconductor and, consequently, robust enough to support excitons. The electronic band structures and their

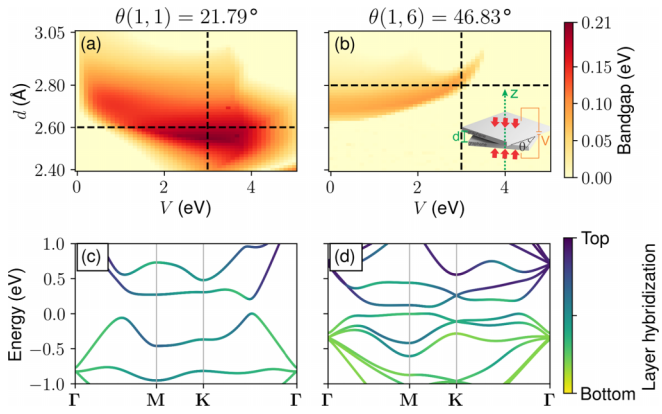

FIG. 3. Electric field and pressure-induced band-gap opening in TBG with a twist angle of (a) $\theta(1,1) = 21.79^\circ$ and (b) $\theta(1,6) = 46.83^\circ$. The corresponding electronic band structures along the path $\mathbf{\Gamma - M - K - \Gamma}$ for the highest gap-opening values for a fixed bias potential of $V = 3$ eV are shown with (c) $E_g \approx 0.18$ eV and (d) $E_g \approx 0.068$ eV, respectively, as marked by the crossing points of the dashed lines with (a) $d = 2.6$ Å and (b) $d = 2.8$ Å. The color map indicates the layer hybridization associated with the bottom-top wave-function composition. The inset in (b) illustrates the TBG under pressure with an interlayer distance d and bias potential V.

layer composition, associated with the spatial localization of the electrons on the individual layers projected in each band for a fixed bias potential $V = 3$ eV, are depicted in Figs. 3(c) and 3(d). In Fig. 3(c), the interlayer distance is $d = 2.6$ Å and the twist angle, $\theta(1,1) = 21.79^\circ$. In Fig. 3(d), on the other hand, we have $d = 2.8$ Å and $\theta(1,6) = 46.83^\circ$. They reveal strong layer hybridization around the bands' edges in both cases. Thus, we will show in latter sections that gapped TBG hosts layered-hybridized moiré excitons. Besides pressure, we could also consider the stretching of TBG layers, not included here, which would increase the interlayer over intralayer hopping ratios, favoring the appearance of a band gap. Recently, it has been demonstrated [26] that the sliding of one graphene layer over the other could open a band gap.

III. DIELECTRIC SCREENING

In Sec. II, the electronic structure of single-particle excitations, considering noninteracting electrons, was described through the tight-binding formalism. To describe exciton formation, we must add many-body interactions to the model, i.e., electron-electron and electron-hole interactions. For this reason, in the current section, we shall derive analytically the static dielectric function of TBG, which will describe how the system is polarized due to the application of an external electric field and how this polarization screens the electrostatic linear response of the system itself. In this work, the dielectric function is calculated in the context of the RPA [37–39] for a periodic system [40,41].

Our goal is to express the dielectric function solely in terms of eigenenergies $E_{n\mathbf{k}}$ and the overlap of the wave functions $u_{n\delta}(\mathbf{k})$ of the unperturbed system, described by the Hamiltonian $\mathcal{H}_0$ present in Sec. II. Such theoretical derivation is based on the works of Refs. [40,41] for layered 2D materials. We will consider that the potential at $\mathbf{k}$ is only affected by $\mathbf{k}' = \mathbf{k}$ and its periodical repetitions, which can be included in our model by restricting the dielectric function to

$$\epsilon^{\ell\ell'}(\mathbf{k},\mathbf{k}') = \sum_{\mathbf{G}_1} \epsilon^{\ell\ell'}(\mathbf{k},\mathbf{k}')\delta_{\mathbf{k}+\mathbf{G}_1,\mathbf{k}'}. \tag{23}$$

The remaining contributions are assumed to average out to zero, which is well justified in the RPA context. In fact, we could go a step further and restrict the screening contributions to the dominant term $\mathbf{G}_1 = 0$ ($\mathbf{k}' = \mathbf{k}$) only, meaning that the dielectric function would be approximated to a local function in momentum space. However, the formulation (23) allows us to be a bit broader and inspect how the terms $\mathbf{G}_1 \neq 0$ affect the screening if necessary. Expanding $\mathbf{k}$ and $\mathbf{k}'$ as $\mathbf{k} = \mathbf{q} + \mathbf{G}$ and $\mathbf{k}' = \mathbf{q}' + \mathbf{G}'$, respectively, with $\mathbf{q}$ and $\mathbf{q}'$ wave vectors restricted to the Brillouin zone, and $\mathbf{G}$ and $\mathbf{G}'$ being the reciprocal lattice vectors, Eq. (23) can be rewritten as

$$\begin{aligned}\epsilon^{\ell\ell'}(\mathbf{q}+\mathbf{G},\mathbf{q}'+\mathbf{G}') &= \sum_{\mathbf{G}_1} \epsilon^{\ell\ell'}(\mathbf{q}+\mathbf{G},\mathbf{q}'+\mathbf{G}')\delta_{\mathbf{q}+\mathbf{G}+\mathbf{G}_1,\mathbf{q}'+\mathbf{G}'} \\ &= \sum_{\mathbf{G}'_1} \epsilon^{\ell\ell'}(\mathbf{q}+\mathbf{G},\mathbf{q}'+\mathbf{G}')\delta_{\mathbf{q}+\mathbf{G}'_1,\mathbf{q}'} \\ &= \epsilon^{\ell\ell'}_{\mathbf{G}\mathbf{G}'}(\mathbf{q})\delta_{\mathbf{q},\mathbf{q}'},\end{aligned} \tag{24}$$

where we defined $\epsilon^{\ell\ell'}_{\mathbf{G}\mathbf{G}'}(\mathbf{q}) = \epsilon^{\ell\ell'}(\mathbf{q}+\mathbf{G},\mathbf{q}+\mathbf{G}')$.

The electronic distribution fluctuations around the ground state are associated with a certain induced potential ϕ_{ind}. To study how excitons are formed in this system, instead of obtaining the exact form of ϕ_{ext}, we will, however, approach this problem by associating a dielectric function that will establish a direct relation between ϕ_{ext} and the total potential $\phi = \phi_{\text{ext}} + \phi_{\text{ind}}$. We treat each carbon site of the TBG as a point charge, such that variations in charge density due to fluctuations on the Fermi sea can be written as

$$\sigma_1(\mathbf{r})\delta(z) + \sigma_2(\mathbf{r})\delta(z-d), \tag{25}$$

where $\sigma_\ell(\mathbf{r})$ is the surface charge density fluctuation of layer ℓ and $\delta(z)$ is the delta function. The induced potential is obtained by the solution of the Poisson equation associated with this charge density,

$$\nabla^2\phi_{\text{ind}}(\mathbf{r},z) = -\frac{1}{\epsilon_0}[\sigma_1(\mathbf{r})\delta(z) + \sigma_2(\mathbf{r})\delta(z-d)]. \tag{26}$$

Fourier transforming Eq. (26), one obtains the solution in momentum space,

$$\phi^\ell_{\text{ind}}(\mathbf{k}) = \sum_{\ell'} X^{\ell\ell'}(k)\sigma_{\ell'}(\mathbf{k}), \tag{27}$$

where $\phi^\ell_{\text{ind}}(\mathbf{k}) = \phi_{\text{ind}}(\mathbf{k}, z_\ell)$ with $z_1 = 0$ and $z_2 = d$, and $X^{\ell\ell'}$ is a term associated to the Coulomb potential without screening,

$$X^{\ell\ell'}(k) = \frac{\delta_{\ell\ell'} + (1-\delta_{\ell\ell'})e^{-kd}}{2\epsilon_0 k}, \tag{28}$$

denominated bare Coulomb potential. This potential acts on the system through the one-body Hamiltonian,

$$\begin{aligned}\mathcal{H}_{\text{ind}} &= -e\sum_{\ell\boldsymbol{\delta}_\ell}\sum_{\mathbf{R}}\phi^{\ell}(\mathbf{R}+\boldsymbol{\delta}_\ell)c^{\dagger}_{\mathbf{R}+\boldsymbol{\delta}_\ell}c_{\mathbf{R}+\boldsymbol{\delta}_\ell}\\ &= -\frac{e}{\mathcal{S}}\sum_{\mathbf{q}}^{\text{BZ}}\sum_{\ell}\sum_{\mathbf{G}}\phi^{\ell}(\mathbf{q}+\mathbf{G})\\ &\quad\times\sum_{\mathbf{k}}^{\text{BZ}}\sum_{nn'}M^{nn'}_{\ell}(\mathbf{k},\mathbf{q},\mathbf{G})a^{\dagger}_{n\mathbf{k}}a_{n'\mathbf{k}+\mathbf{q}},\end{aligned}\tag{29}$$

where $\mathcal{S}$ is the surface area of TBG, and we define the overlap term

$$M^{nn'}_{\ell}(\mathbf{k},\mathbf{q},\mathbf{G}) = \sum_{\boldsymbol{\delta}_\ell} u^{*}_{n\boldsymbol{\delta}_\ell}(\mathbf{k})e^{i\mathbf{G}\cdot\boldsymbol{\delta}_\ell}u_{n'\boldsymbol{\delta}_\ell}(\mathbf{k}+\mathbf{q}).\tag{30}$$

On the other hand, the Liouville equation linearized for slow, adiabatic perturbations ρ_{ind} on the density matrix gives

$$i\hbar\partial_t\rho_{\text{ind}} = [\mathcal{H}_0,\rho_{\text{ind}}]+[\mathcal{H}_{\text{ind}},\rho_0],\tag{31}$$

where ρ_0 is the equilibrium density matrix (given by the Fermi-Dirac statistics). In the static approximation, we have $\partial_t\rho_{\text{ind}}\approx 0$ and

$$\langle n\mathbf{k}|\rho_{\text{ind}}|n'\mathbf{k}+\mathbf{q}\rangle = \frac{f(E_{n\mathbf{k}})-f(E_{n'\mathbf{k}+\mathbf{q}})}{E_{n\mathbf{k}}-E_{n'\mathbf{k}+\mathbf{q}}}\langle n\mathbf{k}|\mathcal{H}_{\text{ind}}|n'\mathbf{k}+\mathbf{q}\rangle.\tag{32}$$

Further details on this last derivation are presented in Appendix B.

The fluctuations in the distribution function are also closely related to the charge density through the equation

$$\sigma_\ell(\mathbf{r}) = -e\sum_{\boldsymbol{\delta}_\ell\mathbf{R}}\delta(\mathbf{r}-\mathbf{R}-\boldsymbol{\delta}_\ell)\langle\mathbf{R}+\boldsymbol{\delta}_\ell|\rho_{\text{ind}}|\mathbf{R}+\boldsymbol{\delta}_\ell\rangle,\tag{33}$$

which is Fourier transformed to

$$\begin{aligned}\sigma_\ell(\mathbf{q}+\mathbf{G}) &= \int d^2\mathbf{r}\,e^{-i\mathbf{k}\mathbf{r}}\sigma_\ell(\mathbf{r})\\ &= -e\sum_{\mathbf{k}}^{\text{BZ}}\sum_{nn'}\left[M^{nn'}_{\ell}(\mathbf{k},\mathbf{q},\mathbf{G})\right]^{*}\\ &\quad\times\langle n\mathbf{k}|\rho_{\text{ind}}|n'\mathbf{k}+\mathbf{q}\rangle.\end{aligned}\tag{34}$$

Plugging Eq. (32) into Eq. (34), then explicitly writing the matrix elements $\langle n\mathbf{k}|\mathcal{H}_{\text{ind}}|n'\mathbf{k}+\mathbf{q}\rangle$ according to Eq. (29), one gets

$$\begin{aligned}\sigma_\ell(\mathbf{q}+\mathbf{G}) &= \frac{e^2}{\mathcal{S}}\sum_{\mathbf{k}}^{\text{BZ}}\sum_{nn'}\left[M^{nn'}_{\ell}(\mathbf{k},\mathbf{q},\mathbf{G})\right]^{*}\\ &\quad\times\frac{f(E_{n\mathbf{k}})-f(E_{n'\mathbf{k}+\mathbf{q}})}{E_{n\mathbf{k}}-E_{n'\mathbf{k}+\mathbf{q}}}\\ &\quad\times\sum_{\ell'}\sum_{\mathbf{G}'}\phi^{\ell'}(\mathbf{q}+\mathbf{G}')M^{nn'}_{\ell'}(\mathbf{k},\mathbf{q},\mathbf{G}').\end{aligned}\tag{35}$$

Merging Eqs. (27) and (35), and rearranging some terms, we get

$$\begin{aligned}\phi^{\ell}_{\text{ind}}(\mathbf{q}+\mathbf{G}) &= \frac{e^2}{\mathcal{S}}\sum_{\ell'\mathbf{G}'}\phi^{\ell'}(\mathbf{q}+\mathbf{G}')\sum_{\ell''}X^{\ell\ell''}(|\mathbf{q}+\mathbf{G}|)\\ &\quad\times\sum_{nn'}\sum_{\mathbf{k}}^{\text{BZ}}\left[M^{nn'}_{\ell''}(\mathbf{k},\mathbf{q},\mathbf{G})\right]^{*}\\ &\quad\times\frac{f(E_{n\mathbf{k}})-f(E_{n'\mathbf{k}+\mathbf{q}})}{E_{n\mathbf{k}}-E_{n'\mathbf{k}+\mathbf{q}}}M^{nn'}_{\ell'}(\mathbf{k},\mathbf{q},\mathbf{G}'),\end{aligned}\tag{36}$$

which establishes a relation between ϕ_{ind} and ϕ solely in terms of the energies $E_{n\mathbf{k}}$ and the overlap of wave functions $u_{n\mathbf{k}}$, both of them associated with the unperturbed system $\mathcal{H}_0$. Putting this aside for a moment, we recall that $\phi=\phi_{\text{ext}}+\phi_{\text{ind}}$ and define the dielectric function as

$$\phi^{\ell}_{\text{ext}}(\mathbf{q}+\mathbf{G}) = \sum_{\ell'\mathbf{G}'}\epsilon^{\ell\ell'}_{\mathbf{G}\mathbf{G}'}(\mathbf{q})\phi^{\ell'}(\mathbf{q}+\mathbf{G}').\tag{37}$$

This allows one to derive another relation between ϕ_{ind} and ϕ,

$$\phi^{\ell}_{\text{ind}}(\mathbf{q}+\mathbf{G}) = \sum_{\ell'\mathbf{G}'}\phi^{\ell'}(\mathbf{q}+\mathbf{G}')\left[\delta_{\ell\ell'}\delta_{\mathbf{G}\mathbf{G}'}-\epsilon^{\ell\ell'}_{\mathbf{G}\mathbf{G}'}(\mathbf{q})\right].\tag{38}$$

Comparing Eqs. (36) and (38), we arrive at the following expression for the dielectric function:

$$\begin{aligned}\epsilon^{\ell\ell'}_{\mathbf{G}\mathbf{G}'}(\mathbf{q}) &= \delta_{\ell\ell'}\delta_{\mathbf{G}\mathbf{G}'}-\frac{e^2}{\mathcal{S}}\sum_{\ell''}\sum_{nn'}\sum_{\mathbf{k}}^{\text{BZ}}X^{\ell\ell''}(|\mathbf{q}+\mathbf{G}|)\\ &\quad\times\left[M^{nn'}_{\ell''}(\mathbf{k},\mathbf{q},\mathbf{G})\right]^{*}\frac{f(E_{n\mathbf{k}})-f(E_{n'\mathbf{k}+\mathbf{q}})}{E_{n\mathbf{k}}-E_{n'\mathbf{k}+\mathbf{q}}}\\ &\quad\times M^{nn'}_{\ell'}(\mathbf{k},\mathbf{q},\mathbf{G}'),\end{aligned}\tag{39}$$

which can be seen as a set of matrix elements indexed by $\{\ell,\mathbf{G}\}$ and $\{\ell',\mathbf{G}'\}$. In the limit of zero temperature, we can rewrite Eq. (39) as

$$\begin{aligned}\epsilon^{\ell\ell'}_{\mathbf{G}\mathbf{G}'}(\mathbf{q}) &= \delta_{\ell\ell'}\delta_{\mathbf{G}\mathbf{G}'}+\frac{e^2}{\mathcal{S}}\sum_{\ell''}\sum_{n_cn_v}\sum_{\mathbf{k}}^{\text{BZ}}X^{\ell\ell''}(|\mathbf{q}+\mathbf{G}|)\\ &\quad\times\left[\frac{\left[M^{n_cn_v}_{\ell''}(\mathbf{k},\mathbf{q},\mathbf{G})\right]^{*}M^{n_cn_v}_{\ell'}(\mathbf{k},\mathbf{q},\mathbf{G}')}{E_{n_c\mathbf{k}}-E_{n_v\mathbf{k}+\mathbf{q}}}\right.\\ &\quad\left.+\frac{\left[M^{n_vn_c}_{\ell''}(\mathbf{k},\mathbf{q},\mathbf{G})\right]^{*}M^{n_vn_c}_{\ell'}(\mathbf{k},\mathbf{q},\mathbf{G}')}{E_{n_c\mathbf{k}+\mathbf{q}}-E_{n_v\mathbf{k}}}\right],\end{aligned}\tag{40}$$

where n_c (n_v) is a band index that only sums over conduction (valence) bands.

At last, we emphasize that for $\mathbf{q}$ of the small norm, i.e., within the long-wavelength regime, the dominant term $\epsilon^{\ell\ell'}_{\mathbf{0}\mathbf{0}}$ can be simplified in light of the Rytova-Keldysh potential [54,55] for 2D systems. In this case, it takes the form

$$\epsilon^{\ell\ell'}_{\mathbf{G}\mathbf{G}'}(\mathbf{q}) \approx \left(\delta_{\ell\ell'}+r^{\ell\ell'}_0 q\right)\delta_{\mathbf{G}\mathbf{0}}\delta_{\mathbf{G}'\mathbf{0}},\tag{41}$$

where $r^{\ell\ell'}_0$ are the screening lengths.

Figure 4 presents color plots of the dielectric function calculated using Eq. (40) restricted to the reciprocal lattice vectors $\mathbf{G}=\mathbf{G}'=\mathbf{0}$ and intralayer contribution $\ell=\ell'=0$, for a biased TBG system with gate potential $V=3$ eV, taking

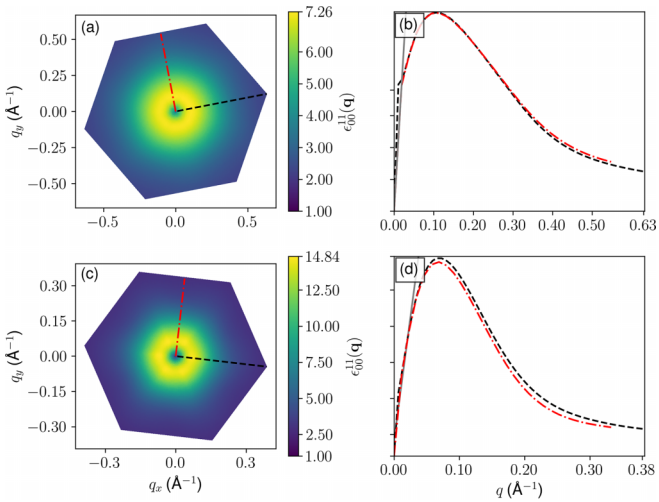

FIG. 4. Dominant term ($\ell = \ell' = 0$, $\mathbf{G} = \mathbf{G}' = \mathbf{0}$) of the dielectric function in momentum space [see Eq. (40)] as a function of the transferred momentum $\mathbf{q}$, calculated in the hexagonal unit cell as shown by the green symbols inside the first Brillouin zone in Fig. 9(b), for a TBG under bias voltage $V = 3$ eV, and twist angles and interlayer distances of (a) $\theta(1,1) = 21.79^\circ$ and $d = 2.6$ Å, and (c) $\theta(1,6) = 46.83^\circ$ and $d = 2.8$ Å. A pronounced ringlike peak is observed in the dielectric function around $(q_x, q_y) = (0,0)$. Cross sections (red and black curves) of the dielectric function's contour plots (a) and (c) are depicted in (b) and (d), respectively, showing linear-fit (gray solid) curves for small $|\mathbf{q}|$.

the twist angle and interlayer distance as $\theta(1,1) = 21.79^\circ$ and $d = 2.6$ Å [Figs. 4(a) and 4(b)], and $\theta(1,6) = 46.83^\circ$ and $d = 2.8$ Å [Figs. 4(c) and 4(d)]. After some inspection, we verified that the $\mathbf{G} = \mathbf{G}' = \mathbf{0}$ contribution is the dominant one, to such an extent that the remaining contributions could be safely neglected in favor of numerical efficiency. From the contour plots of Figs. 4(a) and 4(c), one can observe an almost circularly symmetric ringlike peak for small transferred momenta, exhibiting a linear increasing slope with $|\mathbf{q}|$, as emphasized by the gray solid curve fitting plot of the dielectric function's cross sections in Figs. 4(b) and 4(d). Far from the vicinities of $\mathbf{q} = (0,0)$, the dielectric matrix $\epsilon^{00}_{\mathbf{00}}(\mathbf{q})$ varies slowly, without major fluctuations in its magnitude. Moreover, one verifies that the ringlike peak value oscillates with $\angle\mathbf{q}$.

Given that the $\mathbf{q} = (0, q^{\max}_{y'})$ and $\mathbf{q} = (q^{\max}_{x'}, 0)$ cases maximize the dielectric function at the fixed momentum directions $q_{x'} = 0$ and $q_{y'} = 0$, respectively, where the $(')$ index indicates the rotated momenta directions, we can make estimates about the anisotropy of the dielectric function. For instance, for $\theta(1,6) = 46.83^\circ$ shown in Figs. 4(c) and 4(d), one has the ratios $\epsilon^{00}_{\mathbf{00}}(0, q^{\max}_{y'})/\epsilon^{00}_{\mathbf{00}}(q^{\max}_{x'}, 0) \approx 1.08$ and $q^{\max}_{y'}/q^{\max}_{x'} \approx 1.21$, where the fixed momentum choices are illustrated by the two cross-section curves in black and red dashed lines in Fig. 4(c) and the corresponding direction-dependent peaks shown in Fig. 4(d). These ratios provide a rough quantitative picture of the anisotropy of the dielectric function, which forbade us from simplifying the dielectric function to a $\|\mathbf{q}\|$-dependent function. Despite that, we can verify that the dielectric function presents a linear dependence with respect to $\mathbf{q}$ for small $\|\mathbf{q}\|$ values and goes to 1 at $\mathbf{q} = \mathbf{0}$, in agreement with Eq. (41), as shown by the fit curves (solid gray) in Figs. 4(b) and 4(d). Taking the first-order expansion term of the dielectric function, i.e., by the slope of the fit curves in Figs. 4(b) and 4(d), we obtain $r_0^{00} \approx 208.2$ Å and $r_0^{00} \approx 340.6$ Å for the intralayer contribution with respect to $\theta(1,1) = 21.79^\circ$ and $\theta(1,1) = 46.83^\circ$, respectively. For different cross-section directions, one has that the exact fit value of $r_0^{\ell\ell'}$ is highly dependent on $\angle\mathbf{q}$, which is another anisotropy indicator. Both screening lengths are higher than those of monolayer TMDs [56]. The obtained r_0 values obey the trend reported in Ref. [57] that the smaller the band gap, the higher the screening length.

IV. EXCITONS AND OPTICAL RESPONSE

A. Dielectric screening of the electron-electron interaction

In this section, we follow an approach very analogous to Sec. III, but now treating the potential of any p_z electron in TBG, placed at site $\mathbf{r}_1$ and layer ℓ_1, as an "external" potential acting on another p_z electron placed at site $\mathbf{r}_2$ and layer ℓ_2. We denote this external potential by $\phi_0^{\ell_1\ell_2}(\mathbf{r}_1, \mathbf{r}_2)$ and the screened total potential by $\phi^{\ell_1\ell_2}(\mathbf{r}_1, \mathbf{r}_2)$.

The total potential can be expanded in plane waves by applying the Fourier transform with respect to the real space of $\mathbf{r}_2$ positions,

$$\phi^{\ell_1\ell_2}(\mathbf{r}_1, \mathbf{r}_2) = \frac{1}{\mathcal{S}} \sum_{\mathbf{q}}^{\mathrm{BZ}} \sum_{\mathbf{G}} \phi^{\ell_1\ell_2}(\mathbf{r}_1, \mathbf{q} + \mathbf{G}) e^{\mathrm{i}(\mathbf{q}+\mathbf{G})\cdot\mathbf{r}_2}. \quad (42)$$

Now, introducing the inverse dielectric function through

$$\phi^{\ell_1\ell_2}(\mathbf{r}_1, \mathbf{q} + \mathbf{G}) = \sum_{\ell'\mathbf{G}'} \epsilon^{-1}{}^{\ell_2\ell'}_{\mathbf{G}\mathbf{G}'}(\mathbf{q}) \phi_0^{\ell_1\ell'}(\mathbf{r}_1, \mathbf{q} + \mathbf{G}'), \quad (43)$$

with the relation

$$\sum_{\ell_1\mathbf{G}_1} \epsilon^{\ell\ell_1}_{\mathbf{G}\mathbf{G}_1}(\mathbf{q}) \epsilon^{-1}{}^{\ell_1\ell'}_{\mathbf{G}_1\mathbf{G}'}(\mathbf{q}) = \delta_{\ell\ell'}\delta_{\mathbf{G}\mathbf{G}'}, \quad (44)$$

we obtain

$$\phi^{\ell_1\ell_2}(\mathbf{r}_1, \mathbf{r}_2) = \frac{1}{\mathcal{S}} \sum_{\mathbf{q}}^{\mathrm{BZ}} \sum_{\mathbf{G}} \sum_{\ell'\mathbf{G}'} \epsilon^{-1}{}^{\ell_2\ell'}_{\mathbf{G}\mathbf{G}'}(\mathbf{q}) \times \phi_0^{\ell_1\ell_2}(\mathbf{r}_1, \mathbf{q} + \mathbf{G}') e^{\mathrm{i}(\mathbf{q}+\mathbf{G})\cdot\mathbf{r}_2}. \quad (45)$$

The bare Coulomb potential satisfies $\phi_0^{\ell_1\ell_2}(\mathbf{r}_1, \mathbf{r}_2) = \phi_0^{\ell_1\ell_2}(\mathbf{r}_2 - \mathbf{r}_1)$, which allows us to apply the translation property of the Fourier transform,

$$\phi_0^{\ell_1\ell_2}(\mathbf{r}_1, \mathbf{q} + \mathbf{G}') = \phi_0^{\ell_1\ell_2}(|\mathbf{q} + \mathbf{G}'|) e^{-\mathrm{i}|\mathbf{q}+\mathbf{G}'|\cdot\mathbf{r}_1}, \quad (46)$$

recognizing that the bare Coulomb potential in momentum space is $\phi_0^{\ell_1\ell_2}(|\mathbf{q} + \mathbf{G}|) = -eX^{\ell_1\ell_2}(|\mathbf{q} + \mathbf{G}|)$ [see Eq. (28)]. Replacing Eq. (46) into Eq. (45) results in

$$\phi^{\ell_1\ell_2}(\mathbf{r}_1, \mathbf{r}_2) = -\frac{e}{\mathcal{S}} \sum_{\mathbf{q}}^{\mathrm{BZ}} \sum_{\mathbf{G}\mathbf{G}'} \psi^{\ell_1\ell}_{\mathbf{G}\mathbf{G}'}(\mathbf{q}) e^{\mathrm{i}(\mathbf{q}+\mathbf{G})\cdot\mathbf{r}_2} e^{-\mathrm{i}(\mathbf{q}+\mathbf{G}')\cdot\mathbf{r}_1}, \quad (47)$$

where we defined the screening term

$$\psi^{\ell_1\ell_2}_{\mathbf{G}\mathbf{G}'}(\mathbf{q}) = \sum_{\ell'} \epsilon^{-1}{}^{\ell_2\ell'}_{\mathbf{G}\mathbf{G}'}(\mathbf{q}) X^{\ell_1\ell'}(|\mathbf{q} + \mathbf{G}'|). \quad (48)$$

Then, the interaction between p_z electrons originating from this potential is a two-body operator, written as

$$\mathcal{H}_{\rm ee} = -\frac{e}{2}\sum_{\ell_1\ell_2}\sum_{\boldsymbol{\delta}_{\ell_1}\boldsymbol{\delta}_{\ell_2}}\sum_{\mathbf{R}_1\mathbf{R}_2}\phi^{\ell_1\ell_2}(\mathbf{R}_1+\boldsymbol{\delta}_{\ell_1},\mathbf{R}_2+\boldsymbol{\delta}_{\ell_2}) \times c^{\dagger}_{\mathbf{R}_1+\boldsymbol{\delta}_{\ell_1}}c^{\dagger}_{\mathbf{R}_2+\boldsymbol{\delta}_{\ell_2}}c_{\mathbf{R}_2+\boldsymbol{\delta}_{\ell_2}}c_{\mathbf{R}_1+\boldsymbol{\delta}_{\ell_1}} = \sum_{n_1n_2n_3n_4}\sum_{\mathbf{k}_1\mathbf{k}_2\mathbf{k}_3\mathbf{k}_4}^{\rm BZ} V^{\mathbf{k}_1\mathbf{k}_2\mathbf{k}_3\mathbf{k}_4}_{n_1n_2n_3n_4}a^{\dagger}_{n_1\mathbf{k}_1}a^{\dagger}_{n_2\mathbf{k}_2}a_{n_3\mathbf{k}_3}a_{n_4\mathbf{k}_4}, \quad (49)$$

where the factor of $1/2$ is included to avoid double counting, and we defined the auxiliary term

$$V^{\mathbf{k}_1\mathbf{k}_2\mathbf{k}_3\mathbf{k}_4}_{n_1n_2n_3n_4} = \frac{e^2}{2\mathcal{S}}\sum_{\ell_1\ell_2}\sum_{\mathbf{G}\mathbf{G}'}\psi^{\ell_1\ell_2}_{\mathbf{G}\mathbf{G}'}(\mathbf{k}_1-\mathbf{k}_4) \times\left[M^{n_1n_4}_{\ell_1}(\mathbf{k}_4,\mathbf{k}_1-\mathbf{k}_4,\mathbf{G}')\right]^* \times M^{n_2n_3}_{\ell_2}(\mathbf{k}_2,\mathbf{k}_3-\mathbf{k}_2,\mathbf{G})\delta_{\mathbf{k}_1-\mathbf{k}_4,\mathbf{k}_3-\mathbf{k}_2}. \quad (50)$$

B. Excitonic spectrum

To study the exciton properties using the tight-binding formalism, we employ the semiconductor Bloch equations (SBEs) [42], as explained in detail in Appendix C. The SBE is obtained by writing the Heisenberg equation of motion for the interband transition amplitude $p_{cv}(\mathbf{k}) = \langle\hat{a}^{\dagger}_{c\mathbf{k}}\hat{a}_{v\mathbf{k}}\rangle$, with $\hat{a}_{n\mathbf{k}}$ being the annihilator operator for an electron at the band n with wave number $\mathbf{k}$ for the incidence of an electromagnetic wave with frequency ω and amplitude $\boldsymbol{\mathcal{E}}$. We neglected the Auger process, considering only the highest valence (v) and lowest conduction bands (c), and used the rotating-wave approximation and equilibrium occupation numbers $T = 0$ K. Under all these considerations, the SBE simplifies to

$$(\hbar\omega - \hbar\tilde{\omega}_{\mathbf{k}} + i\gamma)p_{cv}(\mathbf{k}) + \int\frac{d^2\mathbf{q}}{(2\pi)^2}K(\mathbf{k},\mathbf{q})p_{cv}(\mathbf{q}) = \mathbf{d}_{vc}(\mathbf{k})\cdot\boldsymbol{\mathcal{E}}, \quad (51)$$

where $\hbar\tilde{\omega}_{\mathbf{k}}$ is the renormalized transition energy with the inclusion of the exchange self-energy $\hbar\tilde{\omega}_{\mathbf{k}} = E_{c\mathbf{k}} - E_{v\mathbf{k}} + \Sigma_{\mathbf{k}}$, γ is a phenomenological term for the relaxation transition rate, the integral is performed over the first Brillouin zone, $\mathbf{d}_{nm}(\mathbf{k}) = -e\langle n\mathbf{k}|\mathbf{r}|m\mathbf{k}\rangle$ is the dipole moment matrix element, and the kernel $K(\mathbf{k},\mathbf{q})$ is

$$K(\mathbf{k},\mathbf{q}) = e^2\sum_{\ell_1\ell_2}\sum_{\mathbf{G}\mathbf{G}'}\psi^{\ell_1\ell_2}_{\mathbf{G}\mathbf{G}'}(\mathbf{q}-\mathbf{k})\left[M^{cc}_{\ell_1}(\mathbf{k},\mathbf{q}-\mathbf{k},\mathbf{G}')\right]^* \times M^{vv}_{\ell_2}(\mathbf{k},\mathbf{q}-\mathbf{k},\mathbf{G}), \quad (52)$$

with the self-energy $\Sigma_{\mathbf{k}}$ given by

$$\Sigma_{\mathbf{k}} = e^2\sum_{\ell_1\ell_2}\sum_{\mathbf{G}\mathbf{G}'}\int\frac{d^2\mathbf{q}}{(2\pi)^2}\psi^{\ell_1\ell_2}_{\mathbf{G}\mathbf{G}'}(\mathbf{q})\left\{\left[M^{vv}_{\ell_1}(\mathbf{k},\mathbf{q},\mathbf{G}')\right]^* \times M^{vv}_{\ell_2}(\mathbf{k},\mathbf{q},\mathbf{G}) - \left[M^{vc}_{\ell_1}(\mathbf{k},\mathbf{q},\mathbf{G}')\right]^*M^{cv}_{\ell_2}(\mathbf{k},\mathbf{q},\mathbf{G})\right\}. \quad (53)$$

For the calculation of exciton states, we solve the homogeneous version of Eq. (51), setting $\boldsymbol{\mathcal{E}} = \mathbf{0}$ and $\hbar\omega = E_n$ to be the corresponding eigenvalue.

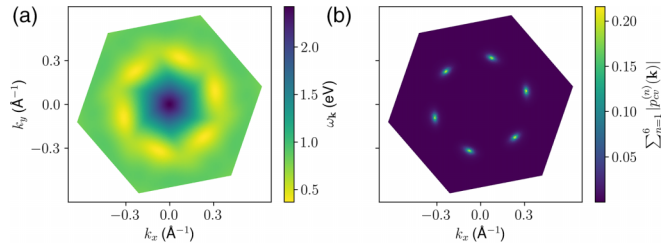

FIG. 5. (a) Renormalized optical band structure, exhibiting a sixfold minimum in the first Brillouin zone of the supercell, and (b) a merging plot of the six first excitonic wave functions in momentum space, located exactly in the optical band edges, for a TBG with $\theta(1,1) = 21.79°$, $V = 3$ eV, and $d = 2.6$ Å.

From the numerically calculated Bloch functions $u_{n\delta_\ell}(\mathbf{k})$ and using the inverse of the dielectric function (40), we obtain the exchange self-energy term and then the renormalized optical band $\hbar\omega_{\mathbf{k}}$. Such results are shown in Fig. 5(a) for $\theta(1,1) = 21.79°$, $V = 3$ eV. As expected, the lower exciton wave functions are localized near the most likely formation points in reciprocal space, i.e., the band-gap points. The renormalization of the band gap was almost of 120 meV, resulting in band gaps up to 364 meV; however, no pronounced qualitative changes were observed on the transition energy $\hbar\omega_{\mathbf{k}}$. From Fig. 5(a), one clearly notices a sixfold minimum in the $\hbar\tilde{\omega}_{\mathbf{k}}$ spectrum located on the band edges along the K-Γ path in the first Brillouin zone of the supercell. In Fig. 5(b), we show the superposition of the six first excitonic wave functions in momentum space, each of them located exactly at one of the six minima of the optical band. They are also strongly anisotropic, spread along the direction orthogonal to the K-Γ path.

The exciton wave functions $\phi_j(\mathbf{k})$ and energies E_j ($j = 1, 2, 3, \ldots$) are obtained by setting the right-hand side of Eq. (51) to zero and solving it as an eigenvalue problem, with eigenenergies $\hbar\omega_{\mathbf{k}} \to E_j$ and eigenfunctions $p_{cv}(\mathbf{k}) \to \phi_j(\mathbf{k})$. Performing such calculations, we show in Figs. 6(a) and 6(b) the first 20 excitonic eigenenergies for (a) $\theta(1,1) = 21.79°$, $V = 3$ eV, and $d = 2.6$ Å and (b) $\theta(1,6) = 46.83°$, $V = 3$ eV and $d = 2.8$ Å. The dashed lines in Figs. 6(a) and 6(b) correspond to the optical band minimum $\min_{\mathbf{k}}\omega_{\mathbf{k}}$ for the assumed sampling $\mathbf{k}$ points. From Figs. 6(a) and 6(b), 12 and 16 excitonic bound states are observed, respectively,

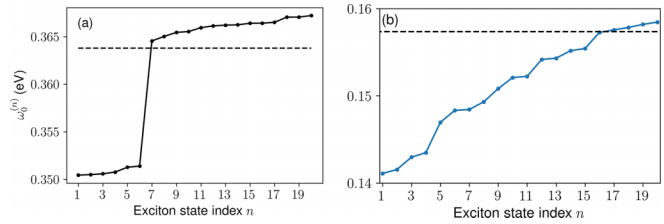

FIG. 6. The first 20th excitonic energies of TBG, taking $N_h = 120$ [see Eq. (19)], for (a) $\theta(1,1) = 21.79°$, $V = 3$ eV, and $d = 2.6$ Å, and (b) $\theta(1,6) = 46.83°$, $V = 3$ eV, and $d = 2.8$ Å. The dashed lines indicate the optical band minima in each case. A clear sixfold degeneracy is observed in (a), in agreement with the C_6 system symmetry.

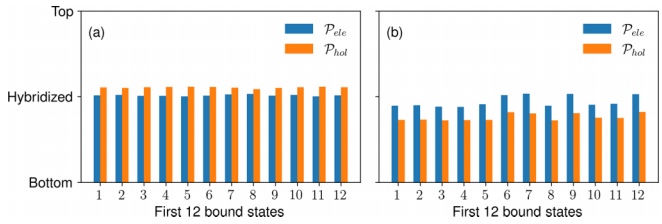

FIG. 7. Bar plot of electron ($\mathcal{P}_{\rm ele}$, blue) and hole ($\mathcal{P}_{\rm hol}$, orange) probabilities of being localized in the top or bottom layers of TBG [see Eqs. (54a) and (54b)], for (a) $\theta(1,1) = 21.79^\circ$, $V = 3$ eV, and $d = 2.6$ Å and (b) $\theta(1,6) = 46.83^\circ$, $V = 3$ eV, and $d = 2.8$ Å. We used $N_{\mathbf{k}} = 8600$ sampling $\mathbf{k}$ points. The probabilities of the first 12 excitonic bound states are close to 0.5, indicating high exciton layer hybridization.

i.e., excitons with energies below the band gap. Figure 6 shows how the convergence of the exciton calculations is highly sensitive on the unit cell number. In fact, for $N_h = 120$, the first configuration [Fig. 6(a)] already exhibits the expected sixfold degeneracy of the ground-state exciton, in agreement with the six equivalent optical band edges shown in Fig. 5(a).

To investigate how the excitons are arranged in TBG, we evaluate the electron and hole layer compositions for the first 12 excitonic bound states. The electron and hole probabilities of each exciton state to be located in the top layer of TBG are given, respectively, by

$$\mathcal{P}_j^{\rm ele} = \sum_{\mathbf{k}}^{\rm BZ} \sum_{\boldsymbol{\delta}_2} |u_{c\boldsymbol{\delta}_2}(\mathbf{k})\phi_j(\mathbf{k})|^2, \tag{54a}$$

$$\mathcal{P}_j^{\rm hol} = \sum_{\mathbf{k}}^{\rm BZ} \sum_{\boldsymbol{\delta}_2} |u_{v\boldsymbol{\delta}_2}(\mathbf{k})\phi_j(\mathbf{k})|^2, \tag{54b}$$

where $u_{v\boldsymbol{\delta}_\ell}(\mathbf{k})$ and $u_{c\boldsymbol{\delta}_\ell}(\mathbf{k})$ are the single-particle electron wave functions for the highest valence and lowest conduction bands, respectively. Probabilities close to 1 (0) indicate electron or hole localization in the top (bottom) layer. However, intermediate values close to 0.5 will indicate the hybridization of the electrons or holes between the TBG layers. In Fig. 7, we show the exciton hybridization between layers for (a) $\theta(1,1) = 21.79^\circ$, $V = 3$ eV, and $d = 2.6$ Å and (b) $\theta(1,6) = 46.83^\circ$, $V = 3$ eV, and $d = 2.8$ Å, evaluated using the probabilities that electrons and holes are localized in one layer or another according to Eqs. (54a) and (54b). As noticed, all excitonic bound states' probabilities are mixed with values close to 0.5, demonstrating that such bound excitons in TBG are strongly layer hybridized, suggesting its interlayer nature, as previously discussed in Figs. 3(c) and 3(d).

From the numerical convergence explained in Appendix D, we found the exciton energy of 350 meV and a binding energy of 13.6 meV. Compared to the few meV binding energies of excitons in bulk materials and hundreds of meV in conventional 2D semiconductors, this result indicates that excitons in TBG are formed with midrange binding energies. It indicates, however, that TBG has potential as a platform for excitons in the midinfrared range.

C. Optical response

To analyze the optical response, we calculate the expectation value of the polarization operator,

$$\langle \mathbf{P} \rangle = -e \sum_{\mathbf{R}\ell\boldsymbol{\delta}_\ell} \left\langle c^\dagger_{\mathbf{R}+\boldsymbol{\delta}_\ell}(t)(\mathbf{R}+\boldsymbol{\delta}_\ell) c_{\mathbf{R}+\boldsymbol{\delta}_\ell}(t) \right\rangle, \tag{55}$$

which can be rewritten using Eqs. (3) and (14) as

$$\langle \mathbf{P} \rangle = \sum_{nn'} \sum_{\mathbf{k}\mathbf{k}'}^{\rm BZ} \mathbf{d}^{\mathbf{k}'\mathbf{k}}_{n'n} p^{\mathbf{k}'\mathbf{k}}_{n'n}, \tag{56}$$

where $\mathbf{d}^{\mathbf{k}'\mathbf{k}}_{n'n} = -e\langle n'\mathbf{k}'|\mathbf{r}|n\mathbf{k}\rangle$ and $p^{\mathbf{k}'\mathbf{k}}_{n'n} = \langle a^\dagger_{n'\mathbf{k}'} a_{n\mathbf{k}}\rangle$. Since we seek the optical response in the energy range of the bound excitons in TBG, close to the band gap, we restrict the band transitions to the dominant term, from the highest valence band to the lowest conduction band. Assuming momentum conservation and linear regime on the frequency domain, the polarization vector becomes

$$\langle \mathbf{P} \rangle = \sum_{\mathbf{k}}^{\rm BZ} \mathbf{d}_{cv}(\mathbf{k}) p_{cv}(\mathbf{k}) e^{i\omega t}. \tag{57}$$

Further details of this derivation are presented in Appendix C.

Now, we decompose the interband transition amplitude into the excitonic basis and a continuum part,

$$p_{cv}(\mathbf{k},\omega) = \sum_j c_j(\omega)\phi_j(\mathbf{k}) + \phi_c(\mathbf{k}), \tag{58}$$

where the dependency on ω is clearly defined and ϕ_c denotes the continuum part, corresponding to the states above the band gap, which are orthogonal to any excitonic state ϕ_j.

Replacing Eq. (58) back into Eq. (51), and using the orthogonality property of the exciton wave function, we arrive at the following expression for the coefficient $c_j(\omega)$:

$$c_j(\omega) = \frac{\mathbf{d}_j \cdot \boldsymbol{\mathcal{E}}}{\hbar\omega - E_j + i\gamma}, \tag{59}$$

where we defined the exciton dipole $\mathbf{d}_j$ moment as

$$\mathbf{d}_j = \sum_{\mathbf{k}} \phi_j^*(\mathbf{k}) \mathbf{d}^{\mathbf{k}\mathbf{k}}_{vc}. \tag{60}$$

Using Eqs. (58)–(60), we can rewrite Eq. (57) as

$$\mathbf{P}(\omega) = \sum_j \frac{(\mathbf{d}_j \cdot \boldsymbol{\mathcal{E}})\mathbf{d}_j^*}{\hbar\omega - E_j + i\gamma}, \tag{61}$$

where $\langle \mathbf{P} \rangle = \mathbf{P}(\omega)e^{i\omega t}$ and $\mathbf{P}(\omega)$ is the polarization vector. Plugging into Eq. (61) the classical electromagnetism relations $\mathbf{J} = \partial_t \mathbf{P}$ and $\mathbf{J} = \sigma(\omega)\cdot\boldsymbol{\mathcal{E}}$, we arrive at the Elliot formula for the optical conductivity tensor,

$$\sigma(\omega) = 4i\hbar\omega\sigma_0 \sum_j \frac{\tilde{\mathbf{d}}_j^* \otimes \tilde{\mathbf{d}}_j}{\hbar\omega - E_j + i\gamma}, \tag{62}$$

where $\otimes$ denotes the outer product, $\sigma_0 = e^2/4\hbar$, and $\tilde{\mathbf{d}}_j \equiv \mathbf{d}_j/e$ the dimensionless exciton dipole moment. The dipole moment is calculated through the expression

$$\mathbf{d}_{n'n}(\mathbf{k}) = ie\frac{\langle n'\mathbf{k}|\nabla_{\mathbf{k}}\mathcal{H}_{\mathbf{k}}|n\mathbf{k}\rangle}{E_{n'\mathbf{k}} - E_{n\mathbf{k}}}, \tag{63}$$

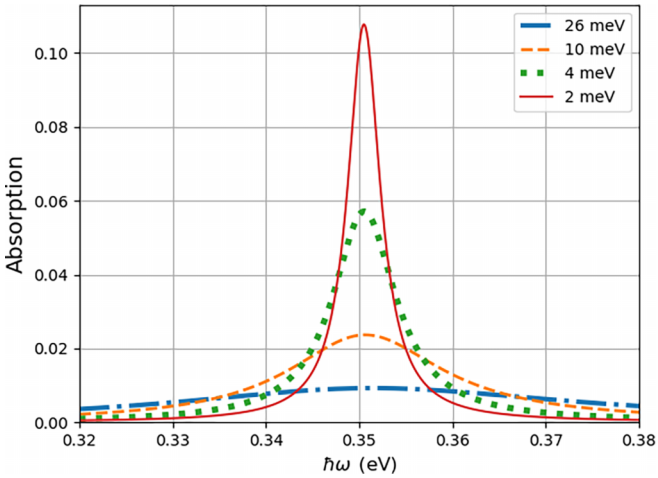

FIG. 8. Light absorption for different values of the relaxation rate γ. The parameters of the TBG are $\theta(1,1) = 21.79°$, $V = 3$ eV, and $d = 2.6$ Å.

where we defined

$$\mathcal{H}_{\mathbf{k}} = \sum_{n} E_{n\mathbf{k}} a^{\dagger}_{n\mathbf{k}} a_{n\mathbf{k}}. \tag{64}$$

Further details of the derivation of the dipole moment are presented in Appendix C.

For bright excitons, reflectance and absorption measurements will show signatures of their presence [58]. From optical conductivity calculations using Eq. (62), one can extract the absorption [59]. We calculated the absorption for a suspended sample, where we include the contribution of the first six degenerated exciton states (see Fig. 5), and we show the results in Fig. 8 for different values of the relaxation rate γ, which represents the effects of disorder and temperature. The absorption increases as the nonradiative decay rate γ decreases, reaching values up to 10% absorption for $\gamma = 2$ meV, a value that is compatible with excitons in TMDs [60]. Thus, we show that optical measurements can probe the presence of excitons in this system.

V. CONCLUSION

In summary, we demonstrated that a band gap can be induced in TBG under pressure for realistic conditions when a voltage bias is applied. In this gapped TBG case, we predicted the existence of highly anisotropic moiré excitons that strongly interact with light. Moreover, the methodology developed here for studying excitons in moiré systems can be applied to other 2D twisted materials.

ACKNOWLEDGMENTS

V.G.M.D. acknowledges financial support from a Msc. scholarship from the Brazilian agency CAPES (Fundação Coordenação de Aperfeiçoamento de Pessoal de Nível Superior). A.J.C., L.K.T, and D.R.d.C. were supported by CNPq (Conselho Nacional de Desenvolvimento Científico e Tecnológico) Grants No. 400789/2019-0, No. 310422/2019-1, No. 316081/2023-0, No. 308486/2015-3, No. 310422/2019-1, No. 315408/2021-9, No. 423423/2021-5, No. 408144/2022-0, and No. 313211/2021-3. N.M.R.P. acknowledges support from the Independent Research Fund Denmark (Grant No. 2032-00045B) and the Danish National Research Foundation (Project No. DNRF165). A.J.C. acknowledges Fundação de Amparo à Pesquisa do Estado de São Paulo (FAPESP) under Grant No. 2022/08086-0, and is grateful to the INL (International Iberian Nanotechnology Laboratory) for the warm hospitality, where part of this work was carried out. The authors also thank LAB-CCAM from ITA for computational support.

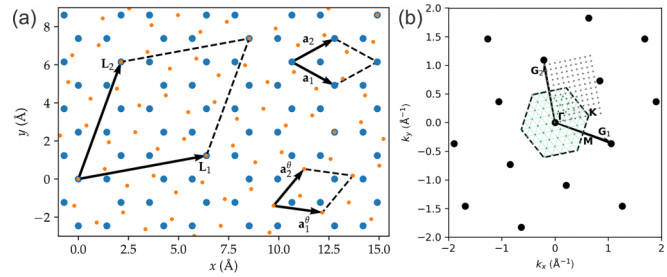

FIG. 9. (a) A top-view schematic representation in real space of TBG for $\theta(1,1) = 21.79°$. Large blue and small orange symbols represent the atoms of the unrotated ($\ell = 1$) and rotated ($\ell = 2$) layers, respectively. The rhombuslike selected unit cell is highlighted using the primitive vectors $\mathbf{L}_1$, $\mathbf{L}_2$, and black dashed lines. The primitive vectors and unit cells of each monolayer are also shown. (b) TBG reciprocal lattice for $\theta(1,1) = 21.79°$. Big black dots denote the lattice vectors $\mathbf{G} = m\mathbf{G}_1 + n\mathbf{G}_2$ ($m, n \in \mathbb{Z}$), where $\mathbf{G}_{1,2}$ are the primitive vectors in the momentum space. The small gray and green dots correspond to the discretized k points of two equivalent first Brillouin zones with rectangular and hexagonal shapes, respectively. For illustrative purposes, unrealistically small values of sampling points were used [see $N_{x',y'}$ in Eq. (18) for the rectangular grid case]. Some high-symmetry points are also indicated: $\mathbf{\Gamma}$, $\mathbf{K}$, $\mathbf{M}$.

APPENDIX A: CRYSTALLOGRAPHIC STRUCTURE

We model a TBG as two planar graphene layers, i.e., buckling effects are neglected. We choose a coordinate system in which the layers are located at $z = 0$ and $z = d$, and thus d is the vertical distance between the layers. Each monolayer graphene lattice is composed of two triangular sublattices, A and B, and their crystalline orientations are rotated relative to each other by an angle θ. Figure 9 shows the TBG lattice from the reference point of an observer looking from above, in the direction $-\mathbf{e}_z$. The sublattice vectors for the unrotated layer ($\ell = 1$ with sublattices A_1 and B_1) and the rotated layer ($\ell = 2$ with sublattices A_2 and B_2) can be explicitly written, respectively, as

$$\mathbf{r}_{A1} = m\mathbf{a}_1 + n\mathbf{a}_2, \tag{A1a}$$

$$\mathbf{r}_{B1} = \mathbf{r}_{A1} + (\mathbf{a}_1 + \mathbf{a}_2)/3, \tag{A1b}$$

$$\mathbf{r}_{A2} = \mathrm{rot}(\theta)\mathbf{r}_{A1} + d\mathbf{e}_z, \tag{A1c}$$

$$\mathbf{r}_{B2} = \mathrm{rot}(\theta)\mathbf{r}_{B1} + d\mathbf{e}_z, \tag{A1d}$$

where $m, n \in \mathbb{Z}$, $\mathbf{a}_{1,2} = a(\sqrt{3}\mathbf{e}_x \mp \mathbf{e}_y)/2$ are the primitive vectors of the ($\ell = 1$)-graphene layer, as depicted in Fig. 9(a), $a = 2.46$ Å is a lattice constant, and $\mathrm{rot}(\theta)$ is the rotation

matrix

$$\mathrm{rot}(\theta) = \begin{bmatrix} \cos\theta & -\sin\theta & 0 \\ \sin\theta & \cos\theta & 0 \\ 0 & 0 & 1 \end{bmatrix}. \tag{A2}$$

The following analysis is restricted to TBG structures with well-defined superlattices and unit cells. In other words, the TBG superlattice must be periodic. This is guaranteed if some atomic positions of different layers match horizontally, which can be written mathematically as

$$m_1\mathbf{a}_1 + n_1\mathbf{a}_2 = m_2\mathbf{a}_1 + n_2\mathbf{a}_2, \tag{A3}$$

for some sets of integers $\{m_1, n_1, m_2, n_2\}$. This Diophantine equation is known as the commensuration condition [45–48]. Its solutions are given in terms of an arbitrary pair of coprime positive integers $\{p, q\}$, such that the possible twist angles between graphene layers are

$$\theta(p,q) = \arccos\left(\frac{3p^2 + 3pq + q^2/2}{3p^2 + 3pq + q^2}\right). \tag{A4}$$

The primitive vectors of the resulting commensurate superlattices are given by

$$\mathbf{L}_1 = \begin{cases} \left(p + \frac{q}{3}\right)\mathbf{a}_1 + \frac{q}{3}\mathbf{a}_2 & \text{if } q \text{ is divisible by 3} \\ p\mathbf{a}_1 + (p+q)\mathbf{a}_2 & \text{otherwise,} \end{cases} \tag{A5a}$$

$$\mathbf{L}_2 = \mathrm{rot}(60^\circ)\mathbf{L}_1. \tag{A5b}$$

Here, we denote by $\mathbf{R} = m\mathbf{L}_1 + n\mathbf{L}_2$ $(m, n \in \mathbb{Z})$ the superlattice vectors and by $\boldsymbol{\delta}_\ell$ the subset of basis vectors of the graphene layer $\ell = \{1, 2\}$ that define the unit cell of the superlattice, as illustrated in Fig. 9(a). Mathematically, $\boldsymbol{\delta}_\ell$ is any lattice vector whose projection in the xy plane can be written as

$$x\mathbf{L}_1 + y\mathbf{L}_2, \ 0 \leqslant x, y < 1. \tag{A6}$$

Any sublattice vector (A1) can be generically rewritten as $\mathbf{R} + \boldsymbol{\delta}_\ell$. The compact notations $\sum_\ell = \sum_{\ell=1}^{2}$, $\sum_{\mathbf{R}}$, and $\sum_{\boldsymbol{\delta}_\ell}$ will be used to indicate sums over all layers, superlattice vectors, and basis vectors, respectively. The reciprocal lattice vectors $\mathbf{G} = m\mathbf{G}_1 + n\mathbf{G}_2$ $(m, n \in \mathbb{Z})$, the reciprocal primitive vectors

$$\mathbf{G}_1 = 2\pi\frac{\mathbf{L}_2 \times \mathbf{e}_z}{|\mathbf{L}_1 \times \mathbf{L}_2|}, \tag{A7a}$$

$$\mathbf{G}_2 = 2\pi\frac{\mathbf{e}_z \times \mathbf{L}_1}{|\mathbf{L}_1 \times \mathbf{L}_2|}, \tag{A7b}$$

and the first Brillouin zone with some of the high-symmetry points (located at the hexagon center $\boldsymbol{\Gamma} = \mathbf{0}$, the vertices $\mathbf{K}$, and the edge midpoints $\mathbf{M}$) are depicted in Fig. 9(b).

APPENDIX B: LIOUVILLE EQUATION

The Liouville equation

$$\mathrm{i}\hbar\partial_t\rho = [\mathcal{H}, \rho] \tag{B1}$$

describes the evolution of a quantum system of particles in terms of the distribution function ρ in phase space associated with a Hamiltonian $\mathcal{H}$. For the unperturbed system, we have $\mathcal{H} = \mathcal{H}_0$ and $\rho = \rho_0$, where ρ_0 is the well-known distribution of the independent electrons' system, which obeys the Pauli exclusion principle. Thus, we can write

$$\rho_0|n\mathbf{k}\rangle = f(E_{n\mathbf{k}})|n\mathbf{k}\rangle, \tag{B2}$$

where $f(E)$ is the Fermi-Dirac distribution,

$$f(E) = \frac{1}{\exp\{(E - E_F)/k_BT\} + 1}, \tag{B3}$$

with k_B being the Boltzmann constant, T the temperature, and E_F the Fermi energy. Notice that as T approaches zero, Eq. (B3) simplifies to

$$f(E) = \begin{cases} 1 \text{ if } E < E_F \\ 1/2 \text{ if } E = E_F \\ 0 \text{ if } E > E_F. \end{cases} \tag{B4}$$

This equation shows that in the ground state ($T = 0$), only the states below the Fermi level (namely, the valence states) are occupied, whereas the states above the Fermi level (namely, the conduction states) are all unoccupied.

The unperturbed distribution ρ_0 commutes with $\mathcal{H}_0$ since they are simultaneously diagonalized by the basis of Bloch states $|n\mathbf{k}\rangle$, as shown in Eqs. (16b) and (B2). For this reason, the unperturbed distribution remains static, and Eq. (B1) simplifies down to

$$\mathrm{i}\hbar\partial_t\rho_0 = [\mathcal{H}_0, \rho_0] = 0. \tag{B5}$$

To explicitly express the matrix elements of ρ_{ind} in the basis $|n\mathbf{k}\rangle$, we recognize that as a first-order approximation, the differential equation (B1) can be linearized by setting ρ_{ind} proportional to the perturbation $\mathcal{H}_{\mathrm{ind}}$. Under this consideration, the commutator $[\mathcal{H}_{\mathrm{ind}}, \rho_{\mathrm{ind}}]$ will vanish, as well as $[\mathcal{H}_0, \rho_0]$ and the time derivative $\partial_t\rho_0$ from Eq. (B5). Thus, one obtains

$$\mathrm{i}\hbar\partial_t\rho_{\mathrm{ind}} = [\mathcal{H}_0, \rho_{\mathrm{ind}}] + [\mathcal{H}_{\mathrm{ind}}, \rho_0]. \tag{B6}$$

The final step is to recognize that in the static approximation, ρ_{ind} will vary slowly. Therefore, setting $\partial_t\rho_{\mathrm{ind}} \approx 0$, it gives

$$\langle n\mathbf{k}|\rho_{\mathrm{ind}}|n'\mathbf{k}+\mathbf{q}\rangle = \frac{f(E_{n\mathbf{k}}) - f(E_{n'\mathbf{k}+\mathbf{q}})}{E_{n\mathbf{k}} - E_{n'\mathbf{k}+\mathbf{q}}}\langle n\mathbf{k}|\mathcal{H}_{\mathrm{ind}}|n'\mathbf{k}+\mathbf{q}\rangle. \tag{B7}$$

APPENDIX C: SEMICONDUCTOR BLOCH EQUATIONS

For this Appendix, we will use a compact notation to soften the burden of the algebraic manipulations and keep the equations reasonably short. First, we will use the compound index $i \equiv \{n_i, \mathbf{k}_i\}$. For even more simplicity, we will write the annihilation and creation operators through the simple notation

$$i \equiv a_{n_i\mathbf{k}_i}. \tag{C1}$$

In addition, we will also consider implicit summations in a similar fashion to Einstein's notation, but only for $i = 3, 4, 5, 6$.

First, we define the full Hamiltonian, written as the sum of three terms,

$$\mathcal{H} = \mathcal{H}_0 + \mathcal{H}_I + \mathcal{H}_{\mathrm{ee}}. \tag{C2}$$

The dipole energy term $\mathcal{H}_I$ is related to the interaction of p_z electrons with the classical electric field $\boldsymbol{\mathcal{E}}$ of the incident light,

$$\mathcal{H}_I = d_{34}3^\dagger 4, \tag{C3}$$

where $d_{34} = \boldsymbol{\mathcal{E}} \cdot \mathbf{d}_{34}$, $\mathbf{d}_{34}$ is the dipole matrix element,

$$\mathbf{d}_{34} = -e\langle 3|\mathbf{r}|4\rangle, \tag{C4}$$

and $\mathbf{r}$ is the position operator. Substituting Eq. (C3) into Eq. (C2) and rewriting the single-particle [Eq. (16b)] and electron-electron [Eq. (49)] Hamiltonians in the compact notation, we obtain

$$\mathcal{H} = E_3 3^\dagger 3 + d_{34}3^\dagger 4 + V_{3456}3^\dagger 4^\dagger 56. \tag{C5}$$

Next, we introduce the Heisenberg equation of motion,

$$-i\hbar\frac{d}{dt}p_{12} = \langle[\mathcal{H}, 1^\dagger 2]\rangle, \tag{C6}$$

where $p_{12} = \langle 1^\dagger 2\rangle$. Substituting Eq. (C5) into Eq. (C6), we get

$$\begin{aligned}-i\hbar\frac{d}{dt}p_{12} =& \langle[E_3 3^\dagger 3, 1^\dagger 2]\rangle + \langle[d_{34}3^\dagger 4, 1^\dagger 2]\rangle \\ &+ \langle[V_{3456}3^\dagger 4^\dagger 56, 1^\dagger 2]\rangle.\end{aligned} \tag{C7}$$

To compute the commutators on the right-hand side, we must apply the anticommutation rules of the fermionic creation and annihilation operators,

$$\{1, 2\} = 0, \tag{C8a}$$

$$\{1^\dagger, 2\} = \delta_{12}. \tag{C8b}$$

Due to the relation (C8a), we also have the property

$$V_{1234} = V_{2143} \tag{C9}$$

and the approximation

$$\langle 1^\dagger 2^\dagger 34\rangle \approx p_{14}p_{23} - p_{13}p_{24}, \tag{C10}$$

which truncates the equation of motion by neglecting three-particle and higher-order terms. Using Eqs. (C8b), (C9), and (C10) to simplify Eq. (C7), it follows that

$$\begin{aligned}-i\hbar\frac{d}{dt}p_{12} =& (E_1 - E_2)p_{12} + d_{31}p_{32} - d_{23}p_{13} \\ &+ 2p_{45}[(V_{3451} - V_{3415})p_{32} \\ &+ (V_{4253} - V_{2453})p_{13}].\end{aligned} \tag{C11}$$

Equation (C11) represents a general form of the SBE, a set of equations whose solutions are the expectation values of the density matrix elements p_{12}. In the scope of this work, we are solely concerned with transitions between the uppermost valence (v) and the lowermost conduction band (c). This is commonly referred to as the two-band approximation. Moreover, momentum is conserved in the electronic transitions since the electric field is homogeneous over all the sample. This allows us to write

$$p_{12} \equiv p^{\mathbf{k}_1\mathbf{k}_2}_{n_1n_2} = p^{\mathbf{k}_1\mathbf{k}_1}_{n_1n_2}\delta_{\mathbf{k}_1\mathbf{k}_2}. \tag{C12}$$

Now we rewrite Eq. (C11) going back to the previous notation and applying Eq. (C12),

$$\begin{aligned}-i\hbar\frac{d}{dt}p^{\mathbf{kk}}_{n_1n_2} =& (E_{n_1\mathbf{k}} - E_{n_2\mathbf{k}})p^{\mathbf{kk}}_{n_1n_2} \\ &+ \sum_{n_3} d^{\mathbf{kk}}_{n_3n_1}p^{\mathbf{kk}}_{n_3n_2} - d^{\mathbf{kk}}_{n_2n_3}p^{\mathbf{kk}}_{n_1n_3} \\ &+ 2\sum_{n_3n_4n_5}\sum_{\mathbf{k}_4}^{\mathrm{BZ}} p^{\mathbf{k}_4\mathbf{k}_4}_{n_4n_5}\big[\big(V^{\mathbf{kk}_4\mathbf{k}_4\mathbf{k}}_{n_3n_4n_5n_1} - V^{\mathbf{kk}_4\mathbf{kk}_4}_{n_3n_4n_1n_5}\big)p^{\mathbf{kk}}_{n_3n_2} \\ &+ \big(V^{\mathbf{k}_4\mathbf{kk}_4\mathbf{k}}_{n_4n_2n_5n_3} - V^{\mathbf{kk}_4\mathbf{k}_4\mathbf{k}}_{n_2n_4n_5n_3}\big)p^{\mathbf{kk}}_{n_1n_3}\big],\end{aligned} \tag{C13}$$

where the summations $\sum_{n_i}$ are restricted to $n_i = c, v$. For the purposes of this work, it will be enough to obtain the solution of the SBE for the matrix element $p^{\mathbf{kk}}_{cv}$. For the dipole energy terms, intraband transitions, i.e., terms with factors of $d^{\mathbf{kk}}_{cc}$ or $d^{\mathbf{kk}}_{vv}$, can be safely neglected. Moreover, terms involving $p^{\mathbf{kk}}_{vc}$ will be neglected in light of the rotating wave approximation (RWA). We also neglect nonlinear terms, i.e., terms where factors of $(p^{\mathbf{kk}}_{n_in_j})^2$ appear. In the end, we remember that the condition of charge neutrality implies $p^{\mathbf{kk}}_{vv} = 1$ and $p^{\mathbf{kk}}_{cc} = 0$. Under all these considerations, Eq. (C13) simplifies to

$$\begin{aligned}-i\hbar\frac{d}{dt}p^{\mathbf{kk}}_{cv} =& (E_{c\mathbf{k}} - E_{v\mathbf{k}})p^{\mathbf{kk}}_{cv} + d^{\mathbf{kk}}_{vc} \\ &+ 2\sum_{\mathbf{k}_4}^{\mathrm{BZ}}\big[p^{\mathbf{kk}}_{cv}\big(V^{\mathbf{kk}_4\mathbf{k}_4\mathbf{k}}_{cvvc} - V^{\mathbf{kk}_4\mathbf{kk}_4}_{cvcv} + V^{\mathbf{k}_4\mathbf{kk}_4\mathbf{k}}_{vvvv} \\ &- V^{\mathbf{kk}_4\mathbf{k}_4\mathbf{k}}_{vvvv}\big) + p^{\mathbf{k}_4}_{cv}\big(V^{\mathbf{kk}_4\mathbf{k}_4\mathbf{k}}_{vcvc} - V^{\mathbf{kk}_4\mathbf{kk}_4}_{vccv}\big)\big].\end{aligned} \tag{C14}$$

Now we recognize the terms

$$\Sigma_{\mathbf{k}} \equiv 2\sum_{\mathbf{k}_4}^{\mathrm{BZ}} V^{\mathbf{kk}_4\mathbf{k}_4\mathbf{k}}_{cvvc} - V^{\mathbf{kk}_4\mathbf{kk}_4}_{cvcv} + V^{\mathbf{k}_4\mathbf{kk}_4\mathbf{k}}_{vvvv} - V^{\mathbf{kk}_4\mathbf{k}_4\mathbf{k}}_{vvvv}, \tag{C15a}$$

$$K(\mathbf{k}, \mathbf{k}_4) \equiv -2\mathcal{S}\big(V^{\mathbf{kk}_4\mathbf{k}_4\mathbf{k}}_{vcvc} - V^{\mathbf{kk}_4\mathbf{kk}_4}_{vccv}\big). \tag{C15b}$$

The term $\Sigma_{\mathbf{k}}$ physically represents the exchange self-energy correction, which corrects the optical band of the system. Using $\Sigma_{\mathbf{k}}$, we write the renormalized optical band as

$$\hbar\tilde{\omega}_{\mathbf{k}} = E_{c\mathbf{k}} - E_{v\mathbf{k}} + \Sigma_{\mathbf{k}}. \tag{C16}$$

The term $K(\mathbf{k}, \mathbf{k}_4)$, on the other hand, is commonly referred to as the kernel of the SBE. Using these definitions, clarifying the dipole energy term $d^{\mathbf{kk}}_{vc} = \boldsymbol{\mathcal{E}} \cdot \mathbf{d}^{\mathbf{kk}}_{vc}$, and considering the linear regime in frequency domain $p^{\mathbf{kk}}_{cv}(t) \approx p^{\mathbf{kk}}_{cv}(\omega)e^{i\omega t}$, where ω is the frequency of oscillation of the electric field, we can rewrite Eq. (C14) as, finally, the final form of our SBE:

$$\hbar(\omega - \tilde{\omega}_{\mathbf{k}})p_{cv}(\mathbf{k}) + \frac{1}{\mathcal{S}}\sum_{\mathbf{q}}^{\mathrm{BZ}} K(\mathbf{k}, \mathbf{q})p_{cv}(\mathbf{q}) = \boldsymbol{\mathcal{E}} \cdot \mathbf{d}_{vc}(\mathbf{k}), \tag{C17}$$

where $p_{cv}(\mathbf{k}) \equiv p^{\mathbf{kk}}_{cv}(\omega)$ and $\mathbf{d}_{vc}(\mathbf{k}) \equiv \mathbf{d}^{\mathbf{kk}}_{vc}$. This is a linear integral equation for $p_{cv}(\mathbf{k})$. Setting the independent term on the right-hand side to zero is equivalent to solving the equation of motion without the dipole energy term, whose solutions will give us the exciton states that the material can host. In this case, $\hbar\omega$ is exchanged by the exciton eigenenergies E_n, and

$p_{cv}(\mathbf{k})$, by the exciton wave functions $\phi_n(\mathbf{k})$, forming an eigenvalue problem [61]. When the dipole energy term is included, however, we will investigate the optical response of the material for incidence of monochromatic light with frequency ω, resulting in an interband transition amplitude $p_{cv}(\mathbf{k})$. Performing the replacement $\hbar\omega \to \hbar\omega + i\gamma$, where γ is a phenomenological term for the relaxation transition rate, and rewriting the summation in $\mathbf{q}$ in the continuum limit $\sum_{\mathbf{q}} \to \mathcal{S}\int d^2\mathbf{q}/(2\pi)^2$, we rewrite the SBE as

$$(\hbar\omega - \hbar\tilde{\omega}_{\mathbf{k}} + i\gamma)p_{cv}(\mathbf{k}) + \int \frac{d^2\mathbf{q}}{(2\pi)^2}K(\mathbf{k},\mathbf{q})p_{cv}(\mathbf{q}) = \boldsymbol{\mathcal{E}}\cdot\mathbf{d}_{vc}(\mathbf{k}). \tag{C18}$$

To simplify the terms (C15) even further, first we notice that terms with factors of the type $V^{\mathbf{k}\mathbf{k}_4\mathbf{k}_4\mathbf{k}}_{n_3n_4n_5n_6}$ can be safely neglected taking into account that for the sums in $\mathbf{G},\mathbf{G}'$, the terms $\mathbf{G}=\mathbf{G}'=\mathbf{0}$ will be exactly compensated by the charged background of ions, and the remaining terms will not have any $\mathbf{q}$ dependence, but will decay as $1/|\mathbf{G}|$ and can be safely neglected. This allows us to write the exchange self-energy and the kernel as

$$\begin{aligned}\Sigma_{\mathbf{k}} &= 2\sum_{\mathbf{q}}^{\mathrm{BZ}} V^{\mathbf{k}+\mathbf{q},\mathbf{k},\mathbf{k}+\mathbf{q},\mathbf{k}}_{vvvv} - V^{\mathbf{k}+\mathbf{q},\mathbf{k},\mathbf{k}+\mathbf{q},\mathbf{k}}_{vcvc}\\ &= e^2\int\frac{d^2\mathbf{q}}{(2\pi)^2}\sum_{\ell_1\ell_2}\sum_{\mathbf{G}\mathbf{G}'}\psi^{\ell_1\ell_2}_{\mathbf{G}\mathbf{G}'}(\mathbf{q})\Big\{\Big[(M^{vv}_{\ell_1}(\mathbf{k},\mathbf{q},\mathbf{G}')\Big]^*\\ &\quad\times M^{vv}_{\ell_2}(\mathbf{k},\mathbf{q},\mathbf{G}) - \Big[M^{vc}_{\ell_1}(\mathbf{k},\mathbf{q},\mathbf{G}')\Big]^* M^{cv}_{\ell_2}(\mathbf{k},\mathbf{q},\mathbf{G})\Big\},\end{aligned} \tag{C19a}$$

$$\begin{aligned}K(\mathbf{k},\mathbf{q}) &= 2\mathcal{S}V^{\mathbf{k}\mathbf{q}\mathbf{k}\mathbf{q}}_{vccv} = 2\mathcal{S}V^{\mathbf{q}\mathbf{k}\mathbf{q}\mathbf{k}}_{cvvc}\\ &= e^2\sum_{\ell_1\ell_2}\sum_{\mathbf{G}\mathbf{G}'}\psi^{\ell_1\ell_2}_{\mathbf{G}\mathbf{G}'}(\mathbf{q}-\mathbf{k})\Big[M^{cc}_{\ell_1}(\mathbf{k},\mathbf{q}-\mathbf{k},\mathbf{G}')\Big]^*\\ &\quad\times M^{vv}_{\ell_2}(\mathbf{k},\mathbf{q}-\mathbf{k},\mathbf{G}).\end{aligned} \tag{C19b}$$

To analyze the optical response, we calculate the expectation value of the polarization operator,

$$\mathbf{P} = -e\sum_{\mathbf{R}\ell\boldsymbol{\delta}_\ell} c^\dagger_{\mathbf{R}+\boldsymbol{\delta}_\ell}(t)(\mathbf{R}+\boldsymbol{\delta}_\ell)c_{\mathbf{R}+\boldsymbol{\delta}_\ell}(t), \tag{C20}$$

with the field operator written as a combination of Eqs. (3) and (14),

$$c^\dagger_{\mathbf{R}+\boldsymbol{\delta}_\ell}(t) = \frac{1}{\sqrt{N}}\sum_n\sum_{\mathbf{k}}^{\mathrm{BZ}} e^{i\mathbf{k}\cdot(\mathbf{R}+\boldsymbol{\delta}_\ell)}u^*_{n\boldsymbol{\delta}_\ell}(\mathbf{k})a^\dagger_{n\mathbf{k}}(t). \tag{C21}$$

Replacing Eq. (C21) into Eq. (C20), the polarization operator becomes

$$\mathbf{P} = -\frac{e}{N}\sum_{nn'}\sum_{\mathbf{k}\mathbf{k}'}^{\mathrm{BZ}}\sum_{\mathbf{R}\ell\boldsymbol{\delta}_\ell} e^{i(\mathbf{k}'-\mathbf{k})\cdot(\mathbf{R}+\boldsymbol{\delta}_\ell)}u^*_{n'\boldsymbol{\delta}_\ell}(\mathbf{k}')u_{n\boldsymbol{\delta}_\ell}(\mathbf{k})\times(\mathbf{R}+\boldsymbol{\delta}_\ell)a^\dagger_{n'\mathbf{k}'}a_{n\mathbf{k}}. \tag{C22}$$

Identifying

$$\langle n'\mathbf{k}'|\mathbf{r}|n\mathbf{k}\rangle = \frac{1}{N}\sum_{\mathbf{R}\ell\boldsymbol{\delta}_\ell} e^{i(\mathbf{k}'-\mathbf{k})(\mathbf{R}+\boldsymbol{\delta}_\ell)}u^*_{n'\boldsymbol{\delta}_\ell}(\mathbf{k}')u_{n\boldsymbol{\delta}_\ell}(\mathbf{k})(\mathbf{R}+\boldsymbol{\delta}_\ell), \tag{C23}$$

we obtain

$$\mathbf{P} = \sum_{nn'}\sum_{\mathbf{k}\mathbf{k}'}^{\mathrm{BZ}}\mathbf{d}^{\mathbf{k}'\mathbf{k}}_{n'n}a^\dagger_{n'\mathbf{k}'}a_{n\mathbf{k}}, \tag{C24}$$

using the dipole moment matrix element definition $\mathbf{d}^{\mathbf{k}'\mathbf{k}}_{n'n} = -e\langle n'\mathbf{k}'|\mathbf{r}|n\mathbf{k}\rangle$. Applying the expectation value operator on Eq. (C24), we get

$$\langle\mathbf{P}\rangle = \sum_{nn'}\sum_{\mathbf{k}\mathbf{k}'}^{\mathrm{BZ}}\mathbf{d}^{\mathbf{k}'\mathbf{k}}_{n'n}p^{\mathbf{k}'\mathbf{k}}_{n'n}. \tag{C25}$$

Using the local approximation (C12) and the linear regime on the frequency domain, we have

$$p^{\mathbf{k}'\mathbf{k}}_{n'n}(t) \approx p^{\mathbf{k}\mathbf{k}}_{n'n}(\omega)\delta_{\mathbf{k}\mathbf{k}'}e^{i\omega t}. \tag{C26}$$

Then,

$$\langle\mathbf{P}\rangle = \sum_{nn'}\sum_{\mathbf{k}}^{\mathrm{BZ}}\mathbf{d}^{\mathbf{k}\mathbf{k}}_{n'n}p^{\mathbf{k}\mathbf{k}}_{n'n}(\omega)e^{i\omega t}. \tag{C27}$$

Since we seek the optical response near the excitonic energy inside the band gap, we shall limit ourselves to the inclusion of the uppermost valence and lowermost conduction bands. Thus,

$$\langle\mathbf{P}\rangle = \sum_{\mathbf{k}}^{\mathrm{BZ}}\mathbf{d}^{\mathbf{k}\mathbf{k}}_{cv}p^{\mathbf{k}\mathbf{k}}_{cv}(\omega)e^{i\omega t}. \tag{C28}$$

Next, we need to expand the dipole moment. For this, we note that

$$\mathbf{r}|\mathbf{R}+\boldsymbol{\delta}_\ell\rangle = (\mathbf{R}+\boldsymbol{\delta}_\ell)|\mathbf{R}+\boldsymbol{\delta}_\ell\rangle, \tag{C29}$$

and so

$$\mathbf{r}|n\mathbf{k}\rangle = \sum_{\mathbf{R},\boldsymbol{\delta}_\ell}(\mathbf{R}+\boldsymbol{\delta}_\ell)e^{i(\mathbf{R}+\boldsymbol{\delta}_\ell)\cdot\mathbf{k}}u_{n\boldsymbol{\delta}_\ell}(\mathbf{k})|\mathbf{R}+\boldsymbol{\delta}_\ell\rangle. \tag{C30}$$

Defining

$$\mathcal{H}_{\mathbf{k}} = \sum_n E_{n\mathbf{k}}|n\mathbf{k}\rangle\langle n\mathbf{k}|, \tag{C31}$$

we have

$$\begin{aligned}[\mathcal{H}_{\mathbf{k}},\mathbf{r}] &= \sum_n E_{n\mathbf{k}}\sum_{\mathbf{R},\boldsymbol{\delta}_\ell}[(\mathbf{R}+\boldsymbol{\delta}_\ell)-(\mathbf{R}'+\boldsymbol{\delta}'_\ell)]\\ &\quad\times e^{i(\mathbf{R}+\boldsymbol{\delta}_\ell)\cdot\mathbf{k}}u_{n\boldsymbol{\delta}_\ell}(\mathbf{k})e^{-i(\mathbf{R}'+\boldsymbol{\delta}'_\ell)\cdot\mathbf{k}}u^*_{n\boldsymbol{\delta}_{\ell'}}(\mathbf{k})\\ &\quad\times|\mathbf{R}+\boldsymbol{\delta}_\ell\rangle\langle\mathbf{R}'+\boldsymbol{\delta}'_{\ell'}|,\end{aligned} \tag{C32}$$

which can be rewritten as

$$\begin{aligned}[\mathcal{H}_{\mathbf{k}},\mathbf{r}] &= -i\nabla_{\mathbf{k}}\mathcal{H}_{\mathbf{k}} - \sum_n\nabla_{\mathbf{k}}(E_{n\mathbf{k}})|\mathbf{k}n\rangle\langle\mathbf{k}n|\\ &\quad-\sum_n\sum_{\mathbf{R},\boldsymbol{\delta}_\ell}\sum_{\mathbf{R}',\boldsymbol{\delta}'_\ell}\nabla_{\mathbf{k}}\Big[u^*_{n\boldsymbol{\delta}_{\ell'}}(\mathbf{k})u_{n\boldsymbol{\delta}_\ell}(\mathbf{k})\Big]\\ &\quad\times e^{-i(\mathbf{R}'+\boldsymbol{\delta}'_\ell)\cdot\mathbf{k}}e^{i(\mathbf{R}+\boldsymbol{\delta}_\ell)\cdot\mathbf{k}}|\mathbf{R}+\boldsymbol{\delta}_\ell\rangle\langle\mathbf{R}'+\boldsymbol{\delta}'_{\ell'}|.\end{aligned} \tag{C33}$$

Now, for $m \neq n$,

$$\langle m\mathbf{k}|[\mathcal{H}_\mathbf{k}, \mathbf{r}]|n\mathbf{k}\rangle = -i\langle m\mathbf{k}|\nabla_\mathbf{k}\mathcal{H}_\mathbf{k}|n\mathbf{k}\rangle - \sum_{n'}\sum_{\mathbf{R},\delta_\ell}\sum_{\mathbf{R}',\delta'_\ell}\nabla_\mathbf{k}\left[u^*_{n'\delta_\ell}(\mathbf{k})u_{n'\delta_\ell}(\mathbf{k})\right] \times u^*_{m\delta_\ell}(\mathbf{k})u_{n\delta'_\ell}, \tag{C34}$$

and we can show that

$$\sum_{n'}\sum_{\mathbf{R},\delta_\ell}\sum_{\mathbf{R}',\delta'_\ell}\nabla_\mathbf{k}\left[u^*_{n'\delta_\ell}(\mathbf{k})u_{n'\delta_\ell}(\mathbf{k})\right]u^*_{m\delta_\ell}(\mathbf{k})u_{n\delta'_\ell} = 0. \tag{C35}$$

Thus,

$$\langle m\mathbf{k}|[\mathcal{H}_\mathbf{k}, \mathbf{r}]|n\mathbf{k}\rangle = -i\langle m\mathbf{k}|\nabla_\mathbf{k}\mathcal{H}_\mathbf{k}|n\mathbf{k}\rangle, \tag{C36}$$

and using that

$$\langle m\mathbf{k}|[\mathcal{H}_\mathbf{k}, \hat{\mathbf{r}}]|n\mathbf{k}\rangle = (E_{m\mathbf{k}} - E_{n\mathbf{k}})\langle m\mathbf{k}|\hat{\mathbf{r}}|n\mathbf{k}\rangle, \tag{C37}$$

we obtain, finally,

$$\mathbf{d}^{\mathbf{k}'\mathbf{k}}_{n'n} = -e\langle n'\mathbf{k}'|\mathbf{r}|n\mathbf{k}\rangle = ie\frac{\langle n'\mathbf{k}'|\nabla_\mathbf{k}\mathcal{H}_\mathbf{k}|n\mathbf{k}\rangle}{E_{n'\mathbf{k}'} - E_{n\mathbf{k}}}. \tag{C38}$$

Notice that the dipole moment satisfies the property $(\mathbf{d}^{\mathbf{k}'\mathbf{k}}_{n'n})^* = \mathbf{d}^{\mathbf{k}\mathbf{k}'}_{nn'}$.

APPENDIX D: NUMERICAL CONVERGENCE

Performing calculations with successively increasing N_h [Eq. (19)], we were able to study the convergence of the band gap and exciton energies with respect to the density of sampled $\mathbf{k}$ points. Since our main interest is to showcase exciton formation in TBG, the discussion is hereafter restricted to one TBG configuration: $\theta(1, 1) = 21.79°$, $V = 3$ eV, and $d = 2.6$ Å. The procedure is entirely analogous to exciton calculations in other gapped TBG configurations, although the convergence may become stiffer due to increased unit cell numbers. The calculations of the band gap $\min_\mathbf{k}\omega_\mathbf{k}$ and ground-state exciton energy E_1, vs $1/N_h$ for several values of N_h, showed a linear trend. Hence, we were able to obtain the energy values for $N_h \to \infty$, namely, the converged values, by verifying the intersection with the vertical axis of linear fits for $\min_\mathbf{k}\omega_\mathbf{k}$ vs $1/N_h$ and E_1 vs $1/N_h$. By performing this procedure, we obtained the converged values of $\min_\mathbf{k}\omega_\mathbf{k} = 364$ meV for the band gap and $E_1 = 350.4$ meV for the first exciton, thus resulting in a binding energy of 13.6 meV.

[1] F. He, Y. Zhou, Z. Ye, S.-H. Cho, J. Jeong, X. Meng, and Y. Wang, ACS Nano **15**, 5944 (2021).
[2] T. Rakib, P. Pochet, E. Ertekin, and H. T. Johnson, J. Appl. Phys. **132**, 120901 (2022).
[3] D. J. Johnson and C. N. Tyson, J. Phys. D **2**, 787 (1969).
[4] Y. Cao, V. Fatemi, S. Fang, K. Watanabe, T. Taniguchi, E. Kaxiras, and P. Jarillo-Herrero, Nature (London) **556**, 43 (2018).
[5] S. Lisi, X. Lu, T. Benschop, T. A. de Jong, P. Stepanov, J. R. Duran, F. Margot, I. Cucchi, E. Cappelli, A. Hunter *et al.*, Nat. Phys. **17**, 189 (2021).
[6] M. I. B. Utama, R. J. Koch, K. Lee, N. Leconte, H. Li, S. Zhao, L. Jiang, J. Zhu, K. Watanabe, T. Taniguchi *et al.*, Nat. Phys. **17**, 184 (2021).
[7] Y. Cao, V. Fatemi, A. Demir, S. Fang, S. L. Tomarken, J. Y. Luo, J. D. Sanchez-Yamagishi, K. Watanabe, T. Taniguchi, E. Kaxiras, R. C. Ashoori, and P. Jarillo-Herrero, Nature (London) **556**, 80 (2018).
[8] A. Weston, E. G. Castanon, V. Enaldiev, F. Ferreira, S. Bhattacharjee, S. Xu, H. Corte-León, Z. Wu, N. Clark, A. Summerfield, T. Hashimoto, Y. Gao, W. Wang, M. Hamer, H. Read, L. Fumagalli, A. V. Kretinin, S. J. Haigh, O. Kazakova, A. K. Geim, V. I. Fal'ko, and R. Gorbachev, Nat. Nanotechnol. **17**, 390 (2022).
[9] T. Song, Q.-C. Sun, E. Anderson, C. Wang, J. Qian, T. Taniguchi, K. Watanabe, M. A. McGuire, R. Stöhr, D. Xiao, T. Cao, J. Wrachtrup, and X. Xu, Science **374**, 1140 (2021).
[10] Y. Xu, K. Kang, K. Watanabe, T. Taniguchi, K. F. Mak, and J. Shan, Nat. Nanotechnol. **17**, 934 (2022).
[11] F. Wu, T. Lovorn, and A. H. MacDonald, Phys. Rev. Lett. **118**, 147401 (2017).
[12] C. Zhang, C.-P. Chuu, X. Ren, M.-Y. Li, L.-J. Li, C. Jin, M.-Y. Chou, and C.-K. Shih, Sci. Adv. **3**, e1601459 (2017).
[13] K. F. Mak, K. He, C. Lee, G. H. Lee, J. Hone, T. F. Heinz, and J. Shan, Nat. Mater. **12**, 207 (2013).
[14] S. Latini, T. Olsen, and K. S. Thygesen, Phys. Rev. B **92**, 245123 (2015).
[15] A. Tartakovskii, Nat. Rev. Phys. **2**, 8 (2020).
[16] K. L. Seyler, P. Rivera, H. Yu, N. P. Wilson, E. L. Ray, D. G. Mandrus, J. Yan, W. Yao, and X. Xu, Nature (London) **567**, 66 (2019).
[17] E. M. Alexeev, D. A. Ruiz-Tijerina, M. Danovich, M. J. Hamer, D. J. Terry, P. K. Nayak, S. Ahn, S. Pak, J. Lee, J. I. Sohn *et al.*, Nature (London) **567**, 81 (2019).
[18] C. Jin, E. C. Regan, A. Yan, M. Iqbal Bakti Utama, D. Wang, S. Zhao, Y. Qin, S. Yang, Z. Zheng, S. Shi *et al.*, Nature (London) **567**, 76 (2019).
[19] K. Tran, G. Moody, F. Wu, X. Lu, J. Choi, K. Kim, A. Rai, D. A. Sanchez, J. Quan, A. Singh *et al.*, Nature (London) **567**, 71 (2019).
[20] H. Yu, G.-B. Liu, J. Tang, X. Xu, and W. Yao, Sci. Adv. **3**, e1701696 (2017).
[21] A. Ciarrocchi, F. Tagarelli, A. Avsar, and A. Kis, Nat. Rev. Mater. **7**, 449 (2022).
[22] T. Ohta, A. Bostwick, T. Seyller, K. Horn, and E. Rotenberg, Science **313**, 951 (2006).
[23] E. V. Castro, K. S. Novoselov, S. V. Morozov, N. M. R. Peres, J. M. B. Lopes dos Santos, J. Nilsson, F. Guinea, A. K. Geim, and A. H. Castro Neto, Phys. Rev. Lett. **99**, 216802 (2007).
[24] Y. Zhang, T.-T. Tang, C. Girit, Z. Hao, M. C. Martin, A. Zettl, M. F. Crommie, Y. R. Shen, and F. Wang, Nature (London) **459**, 820 (2009).
[25] Y. Guo, W. Guo, and C. Chen, Appl. Phys. Lett. **92**, 243101 (2008).
[26] S. Talkington and E. J. Mele, Phys. Rev. B **107**, L041408 (2023).

[27] C.-H. Park and S. G. Louie, Nano Lett. **10**, 426 (2010).
[28] V. V. Cheianov, I. L. Aleiner, and V. I. Fal'ko, Phys. Rev. Lett. **109**, 106801 (2012).
[29] L. Ju, L. Wang, T. Cao, T. Taniguchi, K. Watanabe, S. G. Louie, F. Rana, J. Park, J. Hone, F. Wang, and P. L. McEuen, Science **358**, 907 (2017).
[30] J. C. G. Henriques, I. Epstein, and N. M. R. Peres, Phys. Rev. B **105**, 045411 (2022).
[31] H. Patel, L. Huang, C.-J. Kim, J. Park, and M. W. Graham, Nat. Commun. **10**, 1445 (2019).
[32] Y. H. Kwan, Y. Hu, S. H. Simon, and S. A. Parameswaran, Phys. Rev. Lett. **126**, 137601 (2021).
[33] A. M. van der Zande, J. Kunstmann, A. Chernikov, D. A. Chenet, Y. You, X. Zhang, P. Y. Huang, T. C. Berkelbach, L. Wang, F. Zhang, M. S. Hybertsen, D. A. Muller, D. R. Reichman, T. F. Heinz, and J. C. Hone, Nano Lett. **14**, 3869 (2014).
[34] Y. Tang, J. Gu, S. Liu, K. Watanabe, T. Taniguchi, J. Hone, K. F. Mak, and J. Shan, Nat. Nanotechnol. **16**, 52 (2021).
[35] L. G. Pimenta Martins, D. A. Ruiz-Tijerina, C. A. Occhialini, J.-H. Park, Q. Song, A.-Y. Lu, P. Venezuela, L. G. Cançado, M. S. C. Mazzoni, M. J. S. Matos, J. Kong, and R. Comin, Nat. Nanotechnol. **18**, 1147 (2023).
[36] X. Xie, J. Ding, B. Wu, H. Zheng, S. Li, C.-T. Wang, J. He, Z. Liu, J.-T. Wang, and Y. Liu, Nano Lett. **23**, 8833 (2023).
[37] D. Bohm and D. Pines, Phys. Rev. **82**, 625 (1951).
[38] D. Pines and D. Bohm, Phys. Rev. **85**, 338 (1952).
[39] D. Bohm and D. Pines, Phys. Rev. **92**, 609 (1953).
[40] S. L. Adler, Phys. Rev. **126**, 413 (1962).
[41] N. Wiser, Phys. Rev. **129**, 62 (1963).
[42] M. Kira and S. W. Koch, *Semiconductor Quantum Optics* (Cambridge University Press, Cambridge, 2011).
[43] T. I. Vanhala and L. Pollet, Phys. Rev. B **102**, 035154 (2020).
[44] X.-F. Zhou, Y.-W. Liu, C.-Y. Hao, C. Yan, Q. Zheng, Y.-N. Ren, Y.-X. Zhao, K. Watanabe, T. Taniguchi, and L. He, Phys. Rev. B **107**, 125410 (2023).
[45] J. M. B. Lopes dos Santos, N. M. R. Peres, and A. H. Castro Neto, Phys. Rev. Lett. **99**, 256802 (2007).
[46] E. J. Mele, Phys. Rev. B **81**, 161405(R) (2010).
[47] S. Shallcross, S. Sharma, E. Kandelaki, and O. A. Pankratov, Phys. Rev. B **81**, 165105 (2010).
[48] J. M. B. Lopes dos Santos, N. M. R. Peres, and A. H. Castro Neto, Phys. Rev. B **86**, 155449 (2012).
[49] J. C. Slater and G. F. Koster, Phys. Rev. **94**, 1498 (1954).
[50] P. Moon and M. Koshino, Phys. Rev. B **87**, 205404 (2013).
[51] M. Koshino and P. Moon, J. Phys. Soc. Jpn. **84**, 121001 (2015).
[52] M. Mirzakhani, F. M. Peeters, and M. Zarenia, Phys. Rev. B **101**, 075413 (2020).
[53] A. H. Castro Neto, F. Guinea, N. M. R. Peres, K. S. Novoselov, and A. K. Geim, Rev. Mod. Phys. **81**, 109 (2009).
[54] N. S. Rytova, arXiv:1806.00976 [Moscow Univ. Phys. Bull. **3**, 30 (1967)].
[55] L. V. Keldysh, Sov. J. Exp. Theor. Phys. Lett. **29**, 658 (1979).
[56] T. G. Pedersen, Phys. Rev. B **94**, 125424 (2016).
[57] J.-H. Choi, P. Cui, H. Lan, and Z. Zhang, Phys. Rev. Lett. **115**, 066403 (2015).
[58] Y. Li, A. Chernikov, X. Zhang, A. Rigosi, H. M. Hill, A. M. van der Zande, D. A. Chenet, E.-M. Shih, J. Hone, and T. F. Heinz, Phys. Rev. B **90**, 205422 (2014).
[59] A. J. Chaves, R. M. Ribeiro, T. Frederico, and N. M. R. Peres, 2D Mater. **4**, 025086 (2017).
[60] I. Epstein, B. Terrés, A. J. Chaves, V.-V. Pusapati, D. A. Rhodes, B. Frank, V. Zimmermann, Y. Qin, K. Watanabe, T. Taniguchi, H. Giessen, S. Tongay, J. C. Hone, N. M. R. Peres, and F. H. L. Koppens, Nano Lett. **20**, 3545 (2020).
[61] M. F. C. M. Quintela, J. C. G. Henriques, L. G. M. Tenório, and N. M. R. Peres, Phys. Stat. Sol. (B) **259**, 2200097 (2022).